THE UNIVERSITY OF CHICAGO

TOWARDS THE STUDY OF ULTRAFAST CHIRAL ELECTRONIC DYNAMICS

A DISSERTATION SUBMITTED TO
THE FACULTY OF THE DIVISION OF THE PHYSICAL SCIENCES
IN CANDIDACY FOR THE DEGREE OF
DOCTOR OF PHILOSOPHY

DEPARTMENT OF CHEMISTRY

BY

ELIZABETH M. BAIN

CHICAGO, ILLINOIS

JUNE 2022

This dissertation is dedicated to the grandparents that I wish could be here to see me accomplish this: Catherine Bain, Ben Bain II, and Wayne 'Papa' Kurlinski. I know you all are proud. I love you; rest in peace.

TABLE OF CONTENTS

LIST OF FIGURES

ACKNOWLEDGMENTS

Thank you first, to my parents Ben and Clare Bain for your constant support. Thank you to my brothers Benjamin and David and your families: Courtney, Caitlin, and my wonderful niece and nephew Molly and Rowan for bringing me so much joy. To my Nana, Virginia Kurlinski, thank you for being an incredible example of the kind of woman I want to be. And thank you to my partner Dr. Chloe Avery and our dogs, Maude and Lake for being there for me through most of graduate school and always making life fun. I love you.

Next, thank you to my advisor Prof. Gregory Engel for guiding me through the last 5 years. Thank you for pushing me to be my best and believing in me when I doubted myself. Thank you for giving me the freedom to explore new and exciting ideas and for always supporting me in my goals.

I want to thank the faculty of Wheeling Jesuit University where I obtained my bachelors degree in chemistry, especially Prof. James Coffield, Prof. Mary Railing, Prof. Jason Fuller, and Fr. Michael Steltenkamp. You are all vital parts of my journey to get here. A special thanks to my undergraduate research advisor, Prof. Emily Sylvester. I am forever honored to be your first research student at WJU and am forever grateful for your unending patience and kindness towards me. I have no doubt I would not be writing this thesis without you.

Thank you to other folks from my WJU family who helped get me here. To Nick Cotter for pushing me to come to Chicago to challenge myself. To John Cotter, Dillon McManus, Dr. Anha Lee, Libby Sacco, Mary Meiman, Carly Long, and Sean Shields, thank you for your friendship and support. And thank you to my dear friend Jess Pontis for moving with me to Chicago from West Virginia so I didn't have to start this journey alone. I don't know how I would have gotten through the first couple years without you.

I want to acknowledge my high school chemistry teacher Dan McNally for getting me started on my love of chemistry that led me here.

I want to thank the friends I've made in Chicago as well. Thank you to Maggie Kelty

and Dr. McKenna Goetz for letting me barge into your friendship that first summer picnic. Thank you to Dr. Dan Micheroni and Sarah Willson for being wonderful roommates and friends. Thank you to Prof. Nicole James for many talks in your GCIS office and for being my guide to Portland.

I have to thank my union, Graduate Students United, for being the place that made me feel strong when I was at my weakest. Having that community was vital to my success in graduate school. Thank you especially to Dr. Clara del Junco for reaching out to me and welcoming me into that collective. Graduate students are workers and I believe in the work that we did, and the work that is still ongoing, to make the University of Chicago a better place to be a worker.

I also want to thank the Engel group. A special thanks to Team Chiral: Caitlin Bellora and Dr. Will Hollingsworth. Thank you to the older graduates who mentored me: Dr. Nick Williams, Dr. Lili Wang, Dr. Ryan Wood, Prof. Sara Massey, Dr. John Otto, Dr. Sara Sohail, Dr. Marco Allodi, Dr. Sarah Zinn, Dr. Richard Mazuski, Dr. Polina Navotnaya, and Dr. PoChieh Ting. Thank you to my fellow cohort members Jake Higgins and Lawson LLoyd for starting this crazy ride with me. Thank you to the younger students who I know will carry the lab well into the future: Siddartha Sohoni, Indranil Ghosh, Qijie Shen, Coco Li, Olivia Wedig, and Eric Wu. And a final thanks to the many other members of the group, past and present.

And lastly, I want to acknowledge my committee members Prof. Norbert Scherer and Prof. Andrei Tokmakoff for their indispensable guidance.

ABSTRACT

This dissertation aims to provide new methods of interrogating the nature of electronic dynamics in chiral materials. The superiority of photosynthetic light harvesting over any man-made solar light harvesting devices motivates the study of how chirality affects light harvesting.

A two-dimensional ultrafast chiral spectroscopy is designed and built. This new instrumentation has the capability to provide vital and unique insight into 'handed' electronic dynamics. The theory behind the cancellation of achiral background is described. Great care is taken in the engineering of this instrument to optimize a very small signal against a large background.

A novel approach to two-dimensional electronic spectroscopy in the pump-probe geometry is described. The ability to combine the background-free nature of the BOXCARS geometry with the inherent phase stability of the pump-probe geometry and a temporally separated LO results in a 'best of both worlds' spectrometer.

A new model for the extraction of energy transfer time constants from two-dimensional electronic spectra is described. This method is further extended to the interpretation of two-dimensional circular dichroism spectroscopy. The result is the ability to extract 'handed' energy transfer time constants from a simple three level model.

Lastly, several future direction projects are proposed. First, the study of chiral memory in chiral aggregates of achiral porphyrin monomers. Then, the study of chiral dynamics in quantum dots capped with chiral ligands in the hopes of elucidating more about the origin of the QD's CD signal. Then, an experiment to confirm a theoretically surface specific 2DES technique is proposed. And finally, a novel mixed electronic-Raman experiment is proposed to track the effect of groundstate vibrations on the outcome of photochemical reactions.

CHAPTER 1

INTRODUCTION

1.1 Motivation

Efficiently harvesting the sun's energy has been goal towards which human kind has been working for decades. Many different routes have been taken to realize this goal, from biomimetic organic structures, to solid state semiconductors. Across the board, it is recognized that photosynthesis is still the most efficient light harvesting mechanism we know of, by almost an order of magnitude. Therefore, it makes sense to start with biology as our teacher when it comes to efficiently harvesting sunlight. There are many physical explanations for how evolution has honed this skill so impressively including utlizing downhill energy transfer to drive the movement of an excitation across space [1, 2]. But, this thesis focuses on the fact that all of biology is chiral as a point of interest.

All proteins are made up of amino acid building blocks and amino acids are chiral. If something is chiral, this means that it cannot be superimposed on its own mirror image [3]. It stands to reason that chirality may play a part in how photosynthesis became so efficient. It has even been shown that enantiopure organic photovoltaic devices can show improved conversion efficiencies [4]. Additionally, chiral nanomaterials are of great interest for biomedical, optoelectronic and enantioselective applications [5–8]. The goal of this research is to provide experimental insight into chiral electronic dynamics to aid in the advancement of solar light harvesting technologies.

1.2 Introduction to Spectroscopy

Spectroscopy is the study of light-matter interactions [9]. A light-matter interaction happens when a photon is absorbed or emitted by a material. All of the colors that we can see are a direct consequence of the fact that light absorption is quantized, meaning that only discrete

amounts of energy can be absorbed. This comes from the fact that electrons can only exist in quantized energy levels. So when a photon is absorbed, an electron is promoted a level due to conservation of energy. Therefore, only photons of particular energies will be absorbed by a given material [10].

Not only can the energy from the photons be transferred to and from a material, but it can also be transferred between states on the same molecule, as well as between neighboring molecules. The movement of this energy is generally categorized as coherent or incoherent. Coherent energy transfer is characterized as 'wave-like' and maintains phase across the transfer process [2]. Incoherent energy transfer is characterized as 'hopping' and is generally a somewhat random process governed by probabilities and random walks [11]. Spectroscopists have developed a multitude of different spectroscopies to understand the structure and function of materials based on how light interacts with them. These more complex experiments and their founding theory is described in Chapter 2.

1.3 Circular Dichroism Spectroscopy

Circular dichroism spectroscopy is a steady state measurement which records a spectrum that is the difference between absorption of left hand circularly polarized light (LCP) and right hand circularly polarized light (RCP). The polarization of light is the direction in which the electric field oscillates. For circularly polarized light, this electric field vector actually rotates around the axis of propagation of the wave. This method is one of the main ways we have to understand chiral electronic structure. This signal is only nonzero for molecules which are chiral. This comes from the fact that chiral molecules are circularly birefringent. A birefringent material has a polarization-dependent index of refraction. Thus chiral molecules have a different index of refraction for LCP and RCP. Then as a consequence of the Kramers-Kronig relation [12] they also have a different absorption spectrum for LCP and RCP and thus their difference is nonzero. Achiral molecules, on the other hand, have

no polarization-dependent response when it comes to LCP or RCP. Because chirality is a consequence of molecular arrangement, circular dichroism is widely used as a very sensitive probe of structure. This tool becomes even more impactful when time resolution is added to follow chiral dynamics. An instrument which does just that is described in Chapter 3.

Another well-known characteristic of chiral molecules is their ability to rotate linearly polarized light. This effect is known as Optical Rotatry Dispersion (ORD) and is the dispersive counterpart to CD and therefore contains the same information as CD [13]. The polarization rotation resultant from ORD also can be explained by the circular birefringence of chiral molecules. Because linearly polarized light can be expressed as a superposition of RCP and LCP, these different components will travel at different speeds through a chiral medium due to the differences in their index of refraction. When expressed in the linear polarization basis this delay results in an overall rotation of the linear polarization.

1.3.1 Time-Resolved Chiral Spectroscopy

The steady state measurements of absorptive CD and dispersive ORD are extremely useful techniques but due to the relative small strength of these signals, enhancing the sensitivity of these techniques was vital before time-resolved measurements could be achieved [14]. In order to achieve millisecond time resolution the first Pockels cell was developed for fast switching between LCP and RCP [14]. Briefly, a Pockels cell is an electrically controlled birefringent material that can be triggered to delay orthogonal components of linearly polarized light by $+\frac{\lambda}{4}$ or $-\frac{\lambda}{4}$, which when expressed in the circular polarization basis results in LCP and RCP. This electronic control of polarization allowed millisecond time-resolved CD to be achieved.

One approach to increasing the sensitivity of these experiments was to choose to measure the changing polarization characteristics of an incident light source, rather than the direct measurement of the intensity of the small chiral signal [13, 14]. If a beam of elliptical polarization is incident on a chiral medium, the circular dichroism of that medium will

result in the RCP component of that beam being absorbed a different amount than the LCP component. Thus, if a linear polarizer oriented at the minor axis of the ellipse is placed after the sample, how that intensity differs from a reference beam can be mapped onto the circular dichroism [14]. Small changes in the circular dichroism of the sample will result in significantly larger changes in this measured intensity, making this a more sensitive measurement [14]. Alternatively, the CD and ORD can both be measured through polarization monitoring in an experiment developed by Rhee et al [13]. Briefly, when a linearly polarized coherent femtosecond pulse is incident on a chiral sample its polarization undergoes changes that are caused both by the circular dichroism and circular birefringence of the material. The circular dichroism results in the linear beeam becoming elliptically polarized due to the differential absorption of its RCP and LCP components. The circular birefringence causes the LCP and RCP components to travel at different speeds resulting in an overall rotation of the beam's polarization, a direct result of ORD. By measuring the fields which are parallel and perpendicular to the incident field and heterodyning with a reference pulse, one is able to directly obtain the complex optical activity susceptibility which contains both CD and ORD [13].

Other advances in the picosecond regime have involved pump-probe experiments where the pump is depolarized, and the probe alternates elecronically between RCP and LCP [14–16]. The depolarized pump here is a vital component as a linearly polarized pump at short enough times could cause the experiment to be dominated by linear dichroism signals due to the excited states having memory of the orientation of the first interaction [14]. Advancements in ultrafast laser light sources allowed for these experiments to be performed with picosecond to femtosecond time resolution.

Polarization Gratings

Another way to achieve ultrafast chiral information was to introduce polarization gratings [17–19].This idea stems from transient grating spectoscopy in which two ultrafast laser pulses of the same polarization are incident on a sample at the same time but with different wavevectors such that they have a defined crossing angle. This causes the beams to interfere spatially at the sample, resulting in an intensity grating. A third pulse, called the probe is then able to diffract off this grating, carrying molecular information [19]. Now, when those two initial fields are polarized orthogonal to one another what results is what is called a polarization grating [17]. This grating is a sinusoidal oscillation between RCP and LCP across the sample in space. This grating then only exists for a sample in which there is differential absorption between RCP and LCP. This results in a thermal grating due to nonradiative relaxation, which in turn modulates the index of refraction of the sample which allows the probe to scatter off this dispersive grating in a unique, phase-matched direction [19]. The use of polarization gratings then results in an ultrafast chiral experiment that is background-free.

Two-Dimensional Techniques

All ultrafast chiral techniques discussed up to this point have been only one-dimensional techniques, meaning they have only one axis of frequency resolution. More recent advances in experiment and theory have resulted in opening the door to chiral correlation spectroscopies [3, 20–24]. Correlation spectroscopies allow for two axes of frequency resolution which can be vital in congested spectra. They also allow for the direct monitoring of energy transfer processes. One major theoretical advance was the isolation of the third order chiral signal through linear polarization control of the four fields in four wave mixing (4WM) and three wave mixing (3WM) spectroscopies, both of which allow for two-dimensional experiments [3]. The two-dimensional 4WM experiment has been realized once by Engel and coworkers [21]. This experiment was achieved in a background-free geometry and resulted in a unique insight

in to dynamic exciton delocalization. But there are practical reasons why this experiment has only ever been successful once. This will be discussed in the next section.

1.4 Challenges of Two-Dimensional Circular Dichroism Spectroscopy

There are many reasons why two-dimensional chiral spectroscopy has only been experimentally realized once, one main reason being the small signal strength. The chiral signal is typically orders of magnitude weaker than then its achiral counterpart [14]. When attempting to measure a third-order nonlinear chiral signal, this issue is multiplied. The work in this thesis combats that small signal by performing this experiment in a pump-probe geometry which excites more molecules than a typical BOXCARS geometry. Choosing the pump-probe geometry the presents issues of its own including not being background-free. Attempting to measure a signal as small as the chiral signal on the large background of the probe pulse presents a major challenge. Another issue for small signals is shot-to-shot laser fluctuations which can often dominate pump-probe experiments where consecutive laser shots are used to subtract the probe background. Additionally, any contamination from scatter can overwhelm this small signal. Because the chiral signal is dwarfed by any achiral impurities, the imperfections in commercially available linear polarizers create a major barrier [20]. And lastly, physical interpretation of these complex signals can be extremely difficult without extensive theoretical modeling. The work in this thesis has resulted in viable solutions to each of the many issues presented here. More detailed theoretical descriptions can be found in Chapters 2 and 3. Experimental design and data processing solutions can be found in Chapters 3 and 4. Modeling and data interpretation can be found in Chapter 5.

REFERENCES

[1] Jacob S Higgins, Lawson T Lloyd, Sara H Sohail, Marco A Allodi, John P Otto, Rafael G Saer, Ryan E Wood, Sara C Massey, Po-Chieh Ting, Robert E Blankenship, et al. Photosynthesis tunes quantum-mechanical mixing of electronic and vibrational states to steer exciton energy transfer. *Proceedings of the National Academy of Sciences*, 118(11), 2021.

[2] Gregory S Engel, Tessa R Calhoun, Elizabeth L Read, Tae-Kyu Ahn, Tomáš Mančal, Yuan-Chung Cheng, Robert E Blankenship, and Graham R Fleming. Evidence for wavelike energy transfer through quantum coherence in photosynthetic systems. *Nature*, 446(7137):782–786, 2007.

[3] D. Abramavicius and S. Mukamel. Coherent third-order spectroscopic probes of molecular chirality. *J Chem Phys*, 122(13):134305.

[4] Pierre Josse, Ludovic Favereau, Chengshuo Shen, Sylvie Dabos-Seignon, Philippe Blanchard, Clément Cabanetos, and Jeanne Crassous. Enantiopure versus racemic naphthalimide end-capped helicenic non-fullerene electron acceptors: Impact on organic photovoltaics performance. *Chemistry–A European Journal*, 23(26):6277–6281, 2017.

[5] Junjun Liu, Lin Yang, Ping Qin, Shiqing Zhang, Ken Kin Lam Yung, and Zhifeng Huang. Recent advances in inorganic chiral nanomaterials. *Advanced Materials*, 33(50):2005506, 2021.

[6] Assaf Ben-Moshe, Ayelet Teitelboim, Dan Oron, and Gil Markovich. Probing the interaction of quantum dots with chiral capping molecules using circular dichroism spectroscopy. *Nano letters*, 16(12):7467–7473, 2016.

[7] Urice Tohgha, Kirandeep K Deol, Ashlin G Porter, Samuel G Bartko, Jung Kyu Choi, Brian M Leonard, Krisztina Varga, Jan Kubelka, Gilles Muller, and Milan Balaz. Ligand

induced circular dichroism and circularly polarized luminescence in cdse quantum dots. *ACS nano*, 7(12):11094–11102, 2013.

[8] Liguang Xu, Xiuxiu Wang, Weiwei Wang, Maozhong Sun, Won Jin Choi, Ji-Young Kim, Changlong Hao, Si Li, Aihua Qu, Meiru Lu, et al. Enantiomer-dependent immunological response to chiral nanoparticles. *Nature*, 601(7893):366–373, 2022.

[9] Andrei Tokmakoff. Time dependent quantum mechanics and spectroscopy, 2014.

[10] John S Townsend. *A modern approach to quantum mechanics*. University Science Books, 2000.

[11] Mykyta Onizhuk, Siddhartha Sohoni, Giulia Galli, and Gregory S Engel. Spatial patterns of light-harvesting antenna complex arrangements tune the transfer-to-trap efficiency of excitons in purple bacteria. *The Journal of Physical Chemistry Letters*, 12(29):6967–6973, 2021.

[12] RW Boyd and BR Masters. Nonlinear optics 3rd edn (new york: Academic). 2008.

[13] Hanju Rhee, Seong-Soo Kim, Seung-Joon Jeon, and Minhaeng Cho. Femtosecond measurements of vibrational circular dichroism and optical rotatory dispersion spectra. *ChemPhysChem*, 10(13):2209–2211, 2009.

[14] James W Lewis, Robert A Goldbeck, David S Kliger, Xiaoliang Xie, Robert C Dunn, and John D Simon. Time-resolved circular dichroism spectroscopy: experiment, theory, and applications to biological systems. *The Journal of Physical Chemistry*, 96(13):5243–5254, 1992.

[15] Jan Helbing and Mathias Bonmarin. Vibrational circular dichroism signal enhancement using self-heterodyning with elliptically polarized laser pulses. *The Journal of chemical physics*, 131(17):174507, 2009.

[16] Malte Oppermann, Benjamin Bauer, Thomas Rossi, Francesco Zinna, Jan Helbing, Jérôme Lacour, and Majed Chergui. Ultrafast broadband circular dichroism in the deep ultraviolet. *Optica*, 6(1):56–60, 2019.

[17] John T Fourkas, Rick Trebino, and MD Fayer. The grating decomposition method: A new approach for understanding polarization-selective transient grating experiments. i. theory. *The Journal of chemical physics*, 97(1):69–77, 1992.

[18] Masahide Terazima. A new method for circular dichroism detection using cross-polarized transient grating. *The Journal of Physical Chemistry*, 99(7):1834–1836, 1995.

[19] David W Neyer, Larry A Rahn, David W Chandler, Jon A Nunes, and William G Tong. Circular dichroism spectroscopy using coherent laser-induced thermal gratings. *Journal of the American Chemical Society*, 119(35):8293–8300, 1997.

[20] Jun-Ho Choi, Sangheon Cheon, Hochan Lee, and Minhaeng Cho. Two-dimensional nonlinear optical activity spectroscopy of coupled multi-chromophore system. *Physical Chemistry Chemical Physics*, 10(26):3839–3856, 2008.

[21] A. F. Fidler, V. P. Singh, P. D. Long, P. D. Dahlberg, and G. S. Engel. Dynamic localization of electronic excitation in photosynthetic complexes revealed with chiral two-dimensional spectroscopy. *Nat Commun*, 5:3286.

[22] Darius Abramavicius, Wei Zhuang, and Shaul Mukamel. Probing molecular chirality via excitonic nonlinear response. *Journal of Physics B: Atomic, Molecular and Optical Physics*, 39(24):5051–5066, 2006.

[23] D. I. Holdaway, E. Collini, and A. Olaya-Castro. Isolating the chiral contribution in optical two-dimensional chiral spectroscopy using linearly polarized light. *Opt Express*, 25(6):6383–6401.

[24] D. I. Holdaway, E. Collini, and A. Olaya-Castro. Coherence specific signal detection via chiral pump-probe spectroscopy. *J Chem Phys*, 144(19):194112.

CHAPTER 2

THEORY OF NONLINEAR SPECTROSCOPY

Nonlinear spectroscopy is an important tool in understanding chemical dynamics. It has been developed over the years into many different ordered experiments including the third-order experiments which are the focus of this dissertation. All the many ordered spectroscopies stem from the same basic theoretical origin developed by Mukamel [1], the basics of which will be explained in this chapter. This serves as the theoretical basis on which our spectroscopies are built. This unifying theory has helped spectroscopists communicate the meaning of their findings in a more consistent way [2, 3].

2.1 Density Matrix Formalism

Nonlinear spectroscopy aims to interrogate energetic landscapes and their dynamics. The most obvious place to start when one wants to know about the energetics of a quantum mechanical system is the Schrödinger equation:

$$\hat{H}|\psi\rangle = E|\psi\rangle \tag{2.1}$$

where $\hat{H}$ is the Hamiltonian operator, ψ is the wavefunction which fully describes the state of the system, and E is the eigenvalue which describes the energetics of the system

But, because we want to know about quantum dynamics, we want to add time dependence to equation 2.1:

$$\frac{d}{dt}|\psi(t)\rangle = -\frac{i}{\hbar}\hat{H}(t)|\psi(t)\rangle \tag{2.2}$$

It is convenient to separate the time-dependent portion of the Hamiltonian out such that:

$$\hat{H}(t) = \hat{H}_0 + \hat{V}(t) \tag{2.3}$$

where $\hat{H}_0$ is time-independent and describes the material, and $\hat{V}(t)$ contains the time-dependence in the electric field:

$$\hat{V}(t) = -E(t) \cdot \hat{\mu} \tag{2.4}$$

where $\hat{\mu}$ is the transition dipole operator which is what couples the material to the electric field.

In the semiclassical approximation where the light source is treated classically and the material is treated quantum mechanically, then we say $E(t) = E_0 \cos(\omega t)$ [2].

In our spectroscopy, and in most nonlinear spectroscopies, the sample being studied is an ensemble, not a single quantum mechanical object. Therefore, the wavefunction, ψ is not sufficient to describe the system. We then need to introduce the density matrix which is able to describe statistical mixtures in a way the wavefunction is unable to do.

The density matrix is defined as:

$$\rho \equiv |\psi\rangle\langle\psi| \tag{2.5}$$

where $|\psi\rangle$ is the wavefunction ket and $\langle\psi|$ is its conjugate transpose, the bra. Thus the density matrix is the outer product of the wavefunction with itself.

There are a few rules that govern how the density matrix may behave [4]:

1. When properly normalized, $tr(\rho) = 1$.

2. It is always true that $tr(\rho^2) \leq 1$.

3. For a pure state, $tr(\rho^2) = 1$.

4. The density matrix is always Hermitian, or $\rho_{ij}* = \rho_{ij}$.

5. For the expectation value of some observable, A, $\langle A\rangle = tr(A\rho)$.

Here a pure state refers to one which can be completely described by a wavefunction [5]. A mixed state is then a mixture of pure states, or a statistical mixture [5]. The density matrix is able to describe statistical mixtures because it can also be written as

$$\rho = \sum_s p_s |\psi_s\rangle\langle\psi_s| \tag{2.6}$$

When the density matrix is written this way, it can describe both populations and coherences within the same ensemble. Populations occur when both sides of the density matrix are the same state, $|\psi_i\rangle\langle\psi_i|$. Coherences indicate that the material is in a coherent superposition of two states, $|\psi_i\rangle\langle\psi_j|$. The time evolution of populations usually can be represented by exponential decay functions. Signals which originate from coherences oscillate at the frequency of the energy difference between the two states in superposition.

If one was to write the wavefunction as a sum of multiple wavefunctions, the physical meaning becomes a coherent superposition (a pure state), which is physically distinct from a statistical mixture (a mixed state). Therefore, we want to write equation 2.2 in terms of the density matrix instead of the wavefunction.

$$\frac{d}{dt}\rho = -\frac{i}{\hbar}[\hat{H}, \rho] \tag{2.7}$$

Equation 2.7 is also referred to as the Louiville-von Neumann equation.

When the density matrix is expanded perturbatively we get equation 2.8 for a density matrix of order n. The details of this expansion can be found in reference [2].

$$\rho^{(n)}(t) = -\left(-\frac{i}{\hbar}\right)^n \int_{t_0}^{t} d\tau_n \int_{t_0}^{\tau_n} d\tau_{n-1} \dots \int_{t_0}^{\tau_2} d\tau_1 E(\tau_n)E(\tau_{n-1})\dots E(\tau_1) \tag{2.8}$$

$$\cdot e^{-\frac{i}{\hbar}\hat{H}_0(t-t_0)}[\hat{\mu}(\tau_n), [\hat{\mu}(\tau_{n-1}), \dots [\hat{\mu}(\tau_1), \rho(t_0)] \dots]]e^{+\frac{i}{\hbar}\hat{H}_0(t-t_0)}$$

where

$$\hat{\mu}(t) = e^{+\frac{i}{\hbar}\hat{H}_0(t-t_0)}\hat{\mu}e^{-\frac{i}{\hbar}\hat{H}_o(t-t_0)}$$

The density matrix is what contains the information about the system. Unfortunately, we cannot directly measure the density matrix, we can only indirectly measure the material response to our electric field in the form of the macroscopic polarization, which will be described in the next section.

2.2 Macroscopic Polarization

The observable that we measure in nonlinear spectroscopy is the macroscopic polarization. This polarization occurs when an oscillation of charges in the material is driven by the oscillating electric field of the light interacting with it. The polarization, $P(t)$, is the expectation value of the dipole operator, $\hat{\mu}$, which in terms of the density matrix is written as $P(t) = tr(\hat{\mu}\rho(t)$. Then the nth-order polarization is:

$$P^{(n)}(t) = tr(\hat{\mu}\rho^{(n)}(t)) \tag{2.9}$$

$$= -\left(-\frac{i}{\hbar}\right)^n \int_{t_0}^{t} d\tau_n \int_{t_0}^{\tau_n} d\tau_{n-1} \dots \int_{t_0}^{\tau_2} d\tau_1 E(\tau_n)E(\tau_{n-1})\dots E(\tau_1)$$

$$\langle \hat{\mu}(t)[\hat{\mu}(\tau_n), [\hat{\mu}(\tau_{n-1}), \dots [\hat{\mu}(\tau_1), \rho(t_0)]\dots]]\rangle$$

Then changing our time variables from absolute times to time intervals, we get

$$P^{(n)}(t) = \int_0^{\infty} dt_n \int_0^{\infty} dt_{n-1} \dots \int_0^{\infty} dt_1 \tag{2.10}$$

$$E(t-t_n)E(t-t_n-t_{n-1}\ldots E(t-t_n-\ldots-t_1)R^{(n)}(t_n,\ldots,t_1)$$

Where $R^{(n)}$ is the nth-order nonlinear response function:

$$R^{(n)}(t_n,\ldots,t_1) = -\left(-\frac{i}{\hbar}\right)^n \langle\hat{\mu}(t_n+\ldots+t_1)[\hat{\mu}(t_{n-1}+\ldots+t_1),\ldots[\hat{\mu}(0),\rho(-\infty)]\ldots]\rangle \quad (2.11)$$

which is what contains the information about the dynamics of the system we are interested in. The response function describes how the quantum mechanical material responds to the classical electric field pulses pushing it out of equilibrium. The time delays, t_1 through t_n are what enforce time ordering on the system.

The nonlinear spectroscopy experiments described here are all third-order experiments. The third-order nonlinear polarization is then written as

$$P^{(3)}(t) \propto \int_0^\infty dt_3 \int_0^\infty dt_2 \int_0^\infty dt_1 E_3(t-t_3)E_2(t-t_3-t_2) \quad (2.12)$$

$$\cdot E_1(t-t_3-t_2-t_1)R^{(3)}(t_3,t_2,t_1)$$

with

$$R^{(3)}(t_3,t_2,t_1) \propto -i\langle\hat{\mu}(t_3+t_2+t_1)[\hat{\mu}(t_2+t_1),[\hat{\mu}(t_1),[\hat{\mu}(0),\rho(-\infty)]]]\rangle \quad (2.13)$$

2.2.1 Double Sided Feynman Diagrams

As shown in the previous section the response function can get quite convoluted and long even just for third-order. This is why Feynman diagrams are an elegant way to represent the nonlinear response function diagramatically. Here we describe what the rules are that

govern double sided Feynman diagrams [1, 2].

1. Time moves vertically, increasing from bottom to top.

2. The two vertical lines represent sides of the density matrix. The left side being the bra, and the right side being the ket.

3. Arrows indicate light-matter interactions. An arrow pointing in indicates an excitation, and an arrow pointing out indicates a dexcitation.

4. The sign of the diagram, or pathway, is determined by $(-1)^n$ where n is the number of light-matter interactions on the right (bra) side of the diagram.

5. Because the real part of the electric field contains both positive and negative frequencies, an arrow pointing to the right contributes $E_j e^{-i\omega_j t + ik_j \cdot r}$ to the polarization, and an arrow pointing to the left contributes $E_j^* e^{i\omega_j t - ik_j \cdot r}$.

6. The frequency and wavevector of the emitted signal must be the sum of the frequencies and wavevectors of the input electric fields with their appropriate signs.

7. The last interaction, the emission of the signal, must result in a population state. By convention, the signal arrow is on the left (ket) side and pointing outward.

Double sided Feynman pathways provide a great way to describe features on a transient absorption or 2DES spectrum. An example of a Feynman pathway describing a positive ground state bleach (GSB) pathway can be found in figure 2.1.

2.3 Two-Dimensional Electronic Spectroscopy

Two-dimensional Electronic Spectroscopy (2DES) is a nonlinear optical technique aimed at measuring the dynamics of electronic excited states and their couplings [1, 3, 6, 7]. This

section aims to describe the theoretical origin of the 2DES signal as well as the basics of interpreting a 2DES correlation map.

2.3.1 The Third-order Nonlinear Optical Signal

The 2DES signal is a third-order signal typically measured as intensity (I) and integrated over t_3. The 2DES signal homodyne is shown in equation 2.14.

$$S(t_1, t_2) = \int_0^\infty |E_{sig}^{(3)}(t_3; t_1, t_2)|^2 dt_3 \tag{2.14}$$

Typically the signal electric field, $E_{sig}^{(3)}$, is heterodyned with a local oscillator field, E_{LO}, in which case equation 2.14 becomes equation 2.15.

$$\begin{aligned} S(t_{LO}; t_1, t_2) &\propto \int_0^\infty |E_{LO}(t_3 - t_{LO}) + E_{sig}^{(3)}(t_3; t_2, t_1)|^2 dt_3 \\ &\approx I_{LO} + 2\Re \int_0^\infty \left\{ E_{LO}(t_3 - t_{LO}) \cdot E_{sig}^{(3)}(t_3; t_1, t_2) \right\} dt_3 \end{aligned} \tag{2.15}$$

In the semi-impulsive limit, the envelopes of the femtosecond pulses used to create this signal are considered to be Dirac delta functions [2]. In this case, the signal becomes proportional to the third-order material response:

$$S(t_1, t_2, t_3) \propto E_{LO} \cdot E_{sig}^{(3)} \propto e^{i(\mp\phi_1 \pm \phi_2 + \phi_3 - \phi_{LO})} \sum_n i R_n(t_1, , t_2, t_3) \tag{2.16}$$

where $e^{i\phi}$ is a phase factor.

Typically the information from the 2DEs signal is Fourier transformed over the t_1 and t_3 dimensions so the material response can be looked at as coherence frequency (ω_1), rephasing frequency (ω_3) correlation maps as a function of the waiting time (t_2). After this Fourier transform (and phase acquired is set to zero) equation 2.16 becomes equation 2.17.

$$S(\omega_3, t_2, \omega_1) = \int_0^\infty \int_0^\infty \sum_n iR_n(t_3, t_2, t_1) e^{i\omega_1 t_1} e^{i\omega_3 t_3} dt_1 dt_3 \tag{2.17}$$

2.3.2 Phase-Matching and the Third-Order Signal

Conservation of momentum requires that the wavevector of the signal must be the sum of the wavevectors of the input pulses. The sign of each wavevector depends on which side of the density matrix the light-matter interaction happens on, as well as whether the even results in emission or absorption [8]. Generally, when using double sided Feynman diagrams, an arrow pointing to the right has a positive wavevector, and an arrow pointing to the left has a negative wavevector. As an example, take the double sided Feynman diagram in Figure 2.1. For this material response pathway, the signal would emit in the direction $k_1 - k_2 + k_3$. Another example is given in Figure 2.2. This pathway is very similar to Figure 2.1, except that the coherence during t_1 is evolving phase in the opposite direction. We call the pathway in Figure 2.1 nonrephasing and the pathway in Figure 2.2 rephasing. The rephasing pathway has a different phase-matched direction than the nonrephasing pathway because the wavevectors of the first two interactions change sign: $-k_1 + k_2 + k_3$.

As a consequence of this phase-matching requirement, one can design a 2DES experiment where the signal is emitted in a unique direction and thus can be measured with no background. A beam geometry referred to as BOXCARS accomplishes this [3]. A BOXCARS experiment has the three input beams and the local oscillator oriented on 4 corners of a square box before and after the sample, as shown in Figure 2.3. The nonrephasing signal naturally emits in the direction of the local oscillator but the rephasing signal will go in a different direction [8]. But, one can take advantage of the fact that but switching the order of pulses 1 and 2 one can flip the directions of the rephasing and nonrephasing signals, making a second detector unnecessary [8]. When measuring these signals at separate times, it is then necessary to recombine them to recover the purely absorptive signal using equation 2.18 [2].

$$R_{abs} = \Re(R_{rephasing}(-\omega_1, \omega_3) + R_{nonrephasing}(\omega,\omega_3)) \tag{2.18}$$

Another common geometry for 2DES is the pump probe geometry. This experiment only consists of 2 beams and so is much simpler than the boxcars geometry. Figure 2.4 shows a pump-probe beam geometry 2DES experiment. Because in the pump-probe geometry the wavevectors of the first two pulses are parallel, the rephasing and nonrephasing signals travel in the same direction. This, along with the inherent phase stabilization effect of having collinear pulses means that the signal obtained in pump-probe geometry 2DES is naturally purely absorptive [1, 2, 8]. On the other hand, pump-probe geometry 2DES is unable to separate rephasing and nonrephasing components (without phase cycling capabilities) which can be useful in data interpretation. BOXCARS geometry 2DES is able to separate these but at the cost of phase stability. Because all four beams must interact with different optics at some point in the setup, the phase relationship between the pulses is easily lost to path length fluctuations from vibrations. This means a second experiment is necessary to recover that phase information in order to obtain a purely absorptive spectrum [9].

2.3.3 The 2DES Measurement and Interpretation

When the third-order signal is measured in 2DES, it is done so as a function of the precise timing of three broadband, femtosecond, visible light pulses [3, 9]. The first and third time delays are then Fourier transformed to create a frequency-frequency correlation map. A diagram showing the timing of these pulses and their relationship to the 2D map is found in Figure 2.5. The ω_3 axis is generated by an optical Fourier transform through dispersion off a grating and measurement on an array detector [6]. This domain of the signal is later converted from wavelength to frequency and then Fourier interpolated to be linearly spaced in frequency. The ω_1 axis is Fourier transformed in post-processing.

The ω_1 axis can be interpreted as an excitation frequency axis. This comes from the fact that in the 2DES signal, the ensemble is in a coherence during t_1. Thus, the signal will be oscillating at the frequency of the energy gap between the two electronic states in coherence. This results in the Fourier transform of that signal being interpreted as an excitation frequency spectrum. Similarly, the ensemble is in a coherence during t_3 such that the Fourier transform of the signal during t_3 can be interpreted as a detection spectrum. In other words, ω_1 tells us about where the ensemble started, and ω_3 tells us about where it ended up after some time (t_2) has passed.

On these correlation maps, there are spectral features that are present on the diagonal (where $\omega_1 = \omega_3$) and some that are located off the diagonal (where $\omega_1 \neq \omega_3$) and are called cross peaks. The double-sided Feynman diagram in Figure 2.1 is an example of a diagonal peak. The corresponding response function for that pathway is equation 2.19.

$$R_1(t_1, t_2, t_3) \propto i\mu_{ge}^4 e^{+i\omega_{ge}t_1} e^{-t_1/T_2} e^{-t_2/T_1} e^{-i\omega_{ge}t_3} e^{-t_3/T_2} \tag{2.19}$$

One can see from equation 2.19 that the function is oscillatory and decaying during t_1 and t_3 and simply decaying during t_2. This is consistent with being in a coherence which is dephasing during t_1 and t_3 and in a population state during t_2. Because this function is oscillating at the same frequency (ω_{ge}) in both t_1 and t_3, the feature will lie on the diagonal of the correlation map.

2.4 Conclusions

We have presented an abridged version of the theory developed by Mukamel [1] which describes the origin of two-dimensional optical spectroscopy signals. Starting from time-dependent quantum mechanics and integrating density matrix formalism, we have built up a

theoretically robust way to predict the overall signal from a superposition of many different subensembles, coherent and incoherent. This formalism is extremely useful in understanding how to design and interpret third-order nonlinear techniques, and it provides necessary context for the rest of this thesis.

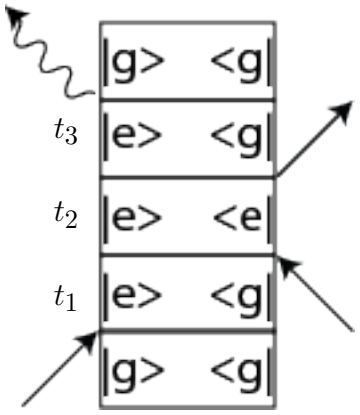

Figure 2.1: Example of a double-sided Feynman diagram. This particular diagram represents a positive ground state bleach response function.

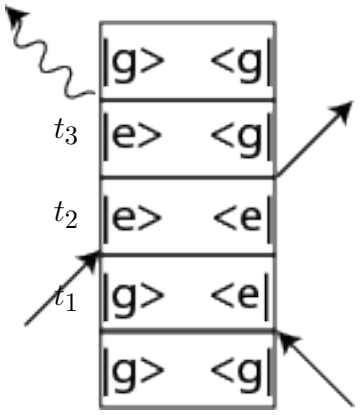

Figure 2.2: An example of a rephasing double sided Feynman diagram. This pathway has a positive sign and physically corresponds to ground state bleach.

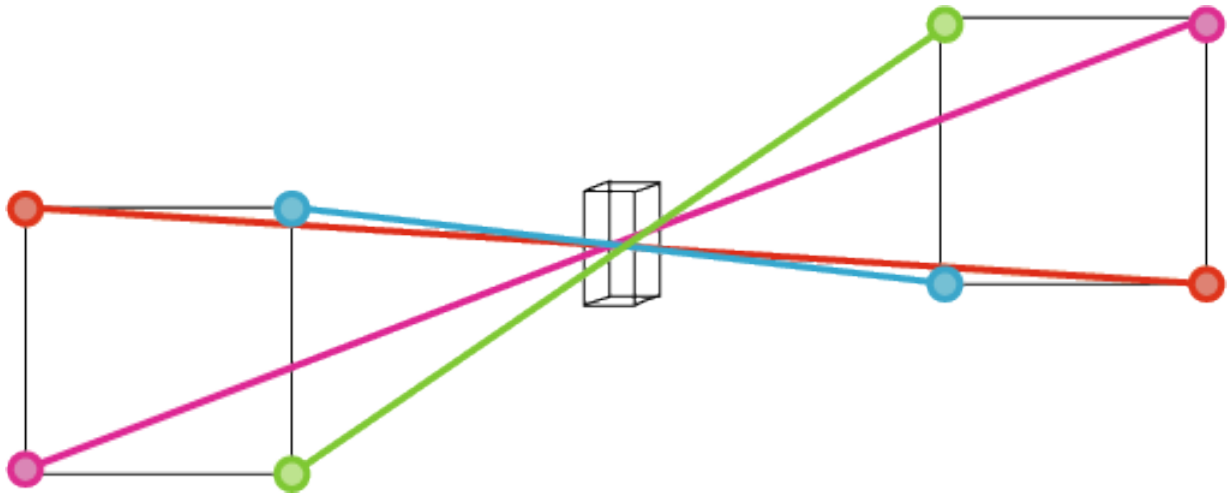

Figure 2.3: Depiction of a BOXCAR geometry 2DES experiment. The three input beams and the local oscillator beam are arranged in a square before and after the sample and overlap in the sample. The measured signal then travels parallel to the local oscillator beam.

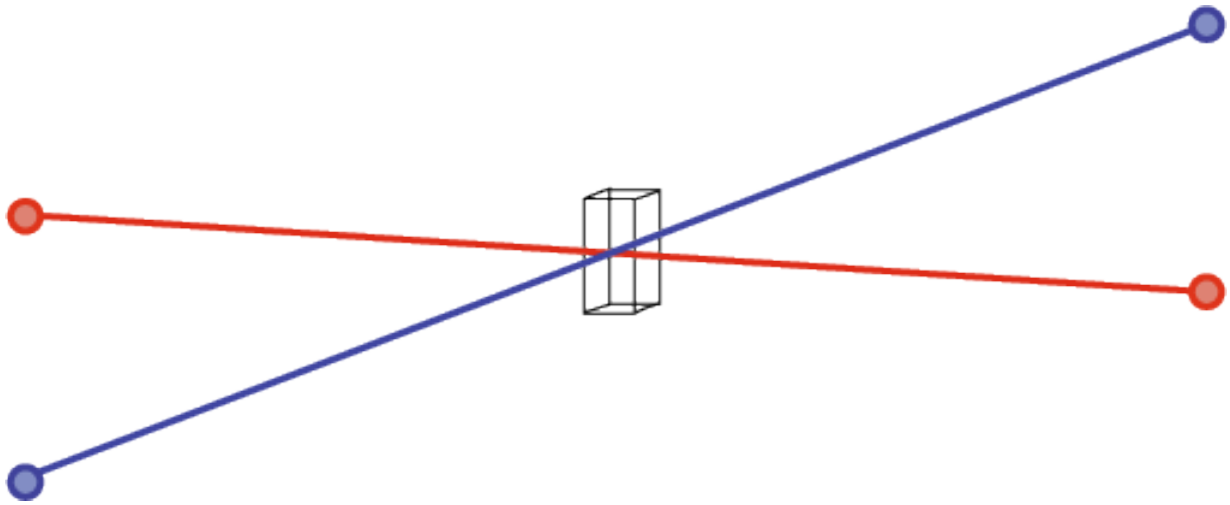

Figure 2.4: Depiction of a pump-probe geometry 2DES experiment. Only two beams are required. One beam contains pulses 1 and 2 collinearly, and the other contains pulse 3 and the signal.

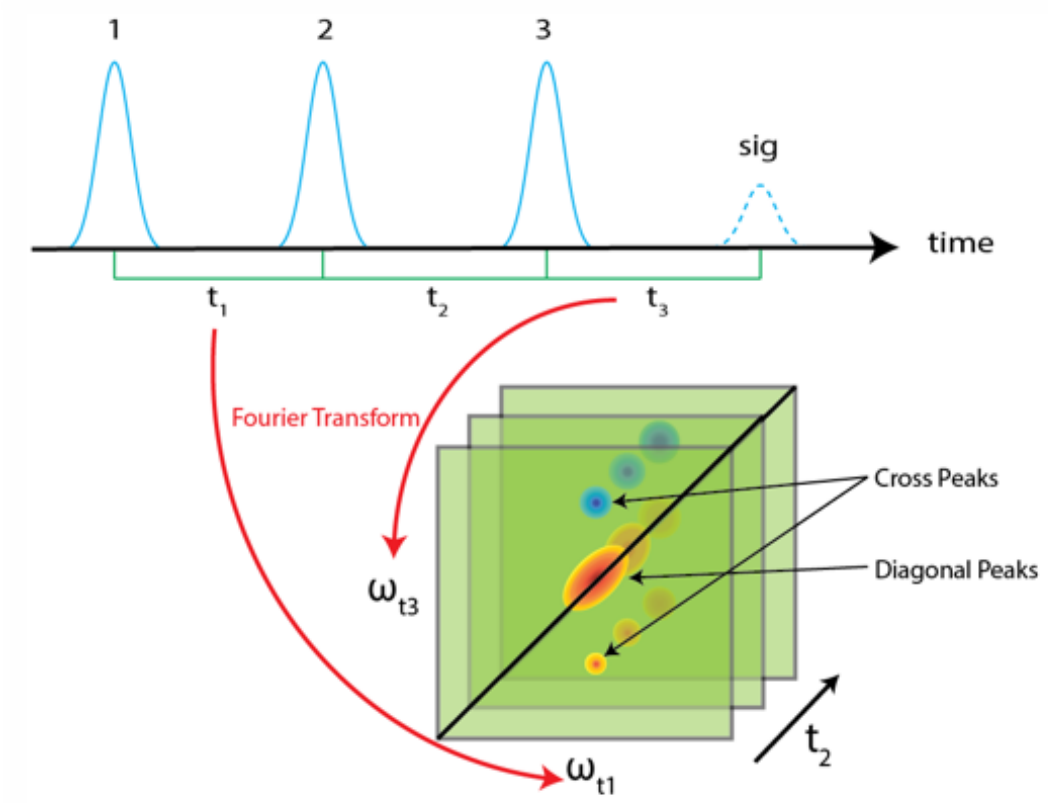

Figure 2.5: Diagram of the 2DES pulse sequence and its relationship with the correlation maps. A series of precisely timed pulses interrogates the sample producing a third-order signal. This signal is dispersed in wavelength off of a grating and then measured on an array detector. This acts as an optical Fourier transform over t_3. The t_1 delay is then Fourier transformed in post-processing, resulting in coherence frequency (ω_1) - rephasing frequency (ω_3) correlation maps at several waiting time (t_2) delays.

REFERENCES

[1] Shaul Mukamel. *Principles of Nonlinear Optical Spectroscopy*. Oxford University Press, New York, 1995.

[2] Peter Hamm and Martin Zanni. *Concepts and Methods of 2D Infrared Spectroscopy*. Cambridge University Press, New York, 2011.

[3] David M Jonas. Two-dimensional femtosecond spectroscopy. *Annual review of physical chemistry*, 54(1):425–463, 2003.

[4] John S Townsend. *A modern approach to quantum mechanics*. University Science Books, 2000.

[5] Ugo Fano. Description of states in quantum mechanics by density matrix and operator techniques. *Reviews of modern physics*, 29(1):74, 1957.

[6] H. Zheng, J. R. Caram, P. D. Dahlberg, B. S. Rolczynski, S. Viswanathan, D. S. Dolzhnikov, A. Khadivi, D. V. Talapin, and G. S. Engel. Dispersion-free continuum two-dimensional electronic spectrometer. *Appl Opt*, 53(9):1909–17.

[7] Elad Harel, Andrew F Fidler, and Gregory S Engel. Real-time mapping of electronic structure with single-shot two-dimensional electronic spectroscopy. *Proceedings of the National Academy of Sciences*, 107(38):16444–16447, 2010.

[8] Andrei Tokmakoff. Time dependent quantum mechanics and spectroscopy, 2014.

[9] John D Hybl, Allison Albrecht Ferro, and David M Jonas. Two-dimensional fourier transform electronic spectroscopy. *The Journal of Chemical Physics*, 115(14):6606–6622, 2001.

CHAPTER 3

TWO-DIMENSIONAL CIRCULAR DICHROISM SPECTROSCOPY

Ultrafast spectroscopy techniques give insight into chemical processes by monitoring quantum dynamics in real time [1–4]. The multitude of information contained in the nonlinear response can result in vital knowledge being lost in the background of spectra. Utilizing polarization control to select for specific tensors of this nonlinear molecular response has been extensively applied to parse the plethora of information contained in multidimensional spectroscopy [5–9]. One such signal that is often lost, and often assumed to be negligible, is the chirality-induced signal [10]. These signals have been shown to be extremely sensitive to structural changes as well as exciton delocalization [11–13].

The difficulty with these experiments lies in the fact that the chirality-induced signal is several orders of magnitude weaker than the electric dipolar signal. Fortunately, the chiral signal can be isolated through precise polarization control, though slight polarization errors can quickly overwhelm the small chiral signal [11, 13]. We have designed two-dimensional circular dichroism spectroscopy to overcome these issues and isolate the chiral signal robustly.

3.1 Theory of the Elimination of the Electric Dipole Contribution

Abramavicius and Mukamel [10, 12, 14] have worked out an elegant way to classify nonlinear signals as chiral or achiral. To determine which signals contain chiral information one needs to use the parity operator, $\mathcal{P}$. This operator performs a space inversion which negates the coordinates of the object such that $x \to -x$, $y \to -y$, and $z \to -z$. For chiral molecules this effectively results in interconversion between enantiomers. Linear circular dichroism spectroscopy is considered parity-odd because it changes sign for ensembles of opposite chirality.

Signals which change sign upon inversion are classified as parity-odd and therefore vanish for achiral samples and racemates, and signals which do not change upon inversion are classified as parity-even. If the molecular response is written in terms of the transition current density, $\mathbf{j}$, we can see which terms contain chiral information:

$$\mathbf{j}_{ma}(-\mathbf{k}) = -i\omega\boldsymbol{\mu}_{ma} - \omega(\mathbf{k}\cdot\mathbf{r}_m)\boldsymbol{\mu}_{ma} - \omega\mathbf{Q}_{ma}\cdot\mathbf{k} + ic\mathbf{k}\times\mathbf{m}_{ma} \tag{3.1}$$

where $\mathbf{k}$ is the wavevector, $\boldsymbol{\mu}$ is the electric transition dipole density, $\mathbf{Q}$ is the electric transition quadrupole density, and $\mathbf{m}$ is the magnetic transition dipole density.

Within the dipole approximation all terms of the third-order response higher than zeroth order in the wavevector, k, are neglected. This results in exclusively electric dipolar terms (first term of equation 3.1) contributing to the signal. Since the electric transition dipole is parity-even, these signals are also parity-even and therefore contain no chiral information. When going beyond the dipole approximation, the molecular response is expanded to include terms which are first order in wavevector (second through fourth terms of equation 3.1). These additional terms are all parity-odd and therefore contain chiral information. The chiral signals can be measured separately from the achiral terms by careful configuration of the wavevector and polarizations of the incident pulses. The next step in developing a chiral third-order experiment is determining the linearly independent tensors of the signal. In order to do this, one must take into account the fact that the sample is isotropic. This is accomplished by applying steps to rotationally average in three dimensions. A procedure developed by Andrews and Thirunamachandran [15] and applied to third-order chiral signals by Abramavicius and Mukamel [10, 12, 14] simplifies this problem to a straightforward matrix formalism. Because the chiral third-order signals are linear in the wavevector, they are three-dimensional tensors of rank five, corresponding to the polarizations of the four fields and the direction of the wavevector. Therefore, we need to use equation 3.2.

$$T^{(5)} = \frac{1}{30} \begin{bmatrix} \epsilon_{v_5 v_4 v_3}\delta_{v_2 v_1} \\ \epsilon_{v_5 v_4 v_2}\delta_{v_3 v_1} \\ \epsilon_{v_5 v_4 v_1}\delta_{v_3 v_2} \\ \epsilon_{v_5 v_3 v_2}\delta_{v_4 v_1} \\ \epsilon_{v_5 v_3 v_1}\delta_{v_4 v_2} \\ \epsilon_{v_5 v_2 v_1}\delta_{v_4 v_3} \end{bmatrix} \begin{bmatrix} 3 & -1 & -1 & 1 & 1 & 0 \\ -1 & 3 & -1 & -1 & 0 & 1 \\ -1 & -1 & 3 & 0 & -1 & -1 \\ 1 & -1 & 0 & 3 & -1 & 1 \\ 1 & 0 & -1 & -1 & 3 & -1 \\ 0 & 1 & -1 & 1 & -1 & 3 \end{bmatrix} \begin{bmatrix} \epsilon_{\alpha_5 \alpha_4 \alpha_3}\delta_{\alpha_2 \alpha_1} \\ \epsilon_{\alpha_5 \alpha_4 \alpha_2}\delta_{\alpha_3 \alpha_1} \\ \epsilon_{\alpha_5 \alpha_4 \alpha_1}\delta_{\alpha_3 \alpha_2} \\ \epsilon_{\alpha_5 \alpha_3 \alpha_2}\delta_{\alpha_4 \alpha_1} \\ \epsilon_{\alpha_5 \alpha_3 \alpha_1}\delta_{\alpha_4 \alpha_2} \\ \epsilon_{\alpha_5 \alpha_2 \alpha_1}\delta_{\alpha_4 \alpha_3} \end{bmatrix} \tag{3.2}$$

where ϵ is the Levi-Civita antisymmetric tensor, δ is the Kronecker delta, v_i is a unit vector in the lab frame, and α_i is a unit vector in the molecular frame.

The left-most vector in equation 3.2 contains information about the field configuration in the lab frame, the square matrix is system independent, and the rightmost vector contains system information in the molecular frame. The lab frame field configuration vector can be rewritten in terms of the four light-matter interactions and the dependent wavevector as shown in equation 3.3. The wavevector is designated as 'dependent' in the case of a noncollinear geometry because the field configuration is only dependent on one wavevector. Seeing as equation 3.3 is a six element column vector, there must be six linearly independent field configurations that satisfy it.

$$F^{(5)}_{\{v\}} = \frac{1}{30} \begin{pmatrix} v_4 \cdot (v_3 \times v_2)(v_1 \cdot v') \\ v_4 \cdot (v_3 \times v_1)(v_2 \cdot v') \\ v_4 \cdot (v_3 \times v')(v_2 \cdot v_1) \\ v_4 \cdot (v_2 \times v_1)(v_3 \cdot v') \\ v_4 \cdot (v_2 \times v')(v_3 \cdot v_1) \\ v_4 \cdot (v_1 \times v')(v_3 \cdot v_2) \end{pmatrix} \tag{3.3}$$

where v_i describe the polarizations of the fields, v' is the dependent wavevector and $v = e_x$, e_y, or e_z are unit vectors in the lab frame.

When restrictions that the electric fields being considered are transverse and that the

signal is x polarized and traveling the z direction are applied, six linearly independent vectors result:

$$yxxx(z) \rightarrow \begin{pmatrix} 0 \\ 0 \\ 0 \\ 0 \\ 0 \\ 1 \end{pmatrix}, xyxx(z) \rightarrow \begin{pmatrix} 0 \\ 0 \\ 0 \\ 0 \\ 1 \\ 0 \end{pmatrix}, xxyx(z) \rightarrow \begin{pmatrix} 0 \\ 0 \\ 1 \\ 0 \\ 0 \\ 0 \end{pmatrix} \tag{3.4}$$

$$zyxx(x) \rightarrow \begin{pmatrix} 0 \\ 0 \\ 0 \\ 1 \\ 0 \\ 0 \end{pmatrix}, xzyx(x) \rightarrow \begin{pmatrix} 1 \\ 0 \\ 0 \\ 0 \\ 0 \\ 0 \end{pmatrix}, zxyx(x) \rightarrow \begin{pmatrix} 0 \\ 1 \\ 0 \\ 0 \\ 0 \\ 0 \end{pmatrix}$$

The notation for the field configuration begins with the polarizations of the fields in the order of their interactions increasing from left to right, followed by the wavevector in parenthesis. For example, the field configuration $yxxx(z)$ signifies that the first field to interact with the sample is polarized in the y direction, while the following two fields and the signal are all polarized in the x direction, and the wavevector is oriented along the z direction.

The second row of tensors then vanish when considering only collinear experiments. When following the pattern of one field being orthogonal to the other three, there is one more tensor which can be expressed as a linear combination of the other three:

$$yyyx(z) \rightarrow \begin{pmatrix} 0 \\ 0 \\ -1 \\ 0 \\ -1 \\ -1 \end{pmatrix} = -yxxx(z) - xyxx(z) - xxyx(z) \tag{3.5}$$

From here on, the dependent wavevector designation will be neglected as we assume the experiment to be performed colinearly.

The $yyyx$ and $xxyx$ ($yxxx$ and $xyxx$) tensors are considered "chiral probe" ("chiral pump") experiments as the chiral resolution is found on the detection (excitation) axis of the spectrum. This chiral resolution can be interpreted as circular dichroism, or LCP-RCP excitation or detection. The tensors' linear independence along with equation 3.5 imply that each of the two pumps or probes contain different physical information.

It is useful to think about the chiral pump sequence as a transient grating experiment. Figure 3.1 depicts how orthogonally polarized fields crossing at an angle can produce a "chiral grating" [16–18]. This comes from the fact that portions of the sample will experience LCP or RCP depending on whether the x or y polarized beam is incident on the sample first. In reality, the picture in Figure 3.1 is a bit simplified. The spatial phase variation across the sample will actually cause a continuous sinusoidal transition betwen RCP and LCP passing through 45 degree linearly polarized light [17]. Work by Fourkas et al [17] has shown that this polarization grating can be broken down into four different intensity gratings: RCP and LCP intensity gratings which are exactly out of phase with one another, and $+45$ and -45 degree linearly polarized intensity gratings that are exactly out of phase with one another and just $\frac{\pi}{2}$ shifted from the RCP and LCP gratings. Because the linearly polarized gratings are out of phase with one another, the only way that signal could arise from them is if there

is differential absorption between the +45 and −45 degree polarized light, in other words, if linear dichroism present in the sample. Because the sample is isotropic, there can be no linear dichroism. Similarly, because the RCP and LCP gratings are our of phase with one another, there can only be a signal if there is differential absorption between RCP and LCP, which is circular dichroism. Thus, the only signal that can result from this field configuration with an isotropic sample is a circular dichroism signal.

One potential issue that arises with this picture is the fact that this is a volume grating, and so our two-dimensional picture is not fully accurate. In fact, due to ORD, the linear polarizations of the beams will rotate as they go through the chiral sample, which could scramble the polarization purity and result in artifacts [19]. The instrument described here, along with most nonlinear spectroscopic instruments that are built in a transmissive geometry, use a very short pathlength of 200μm and low optical density samples to minimize reabsorption of the signal, which in turn helps to minimize these polarization impurities as well.

In this picture of the chiral signal, one might conclude that the difference between the two possible chiral pump sequences might just be a 180 degree phase shift (a sign change). This statement is true, but only at $t_1 = 0$ because that is the only time at which this chiral grating picture is accurate. The physical interpretation of the uniqueness of these signals at $t_1 \neq 0$ is a natural question. In some cases, it is more useful to describe the signal in the x, y basis instead of the RCP,LCP basis. Take the chiral pumps for example: in $yxxx$, the first interaction with the sample selects for transitions that project onto the y axis, then the second interaction projects everything onto the x axis. In $xyxx$, the reverse is true and intuitively the first two interactions interrogate the same physics just rotated 90 degrees. It is when the third and fourth pulses enter the picture that the difference becomes apparent. For $yxxx$, the third interaction is parallel to the second, while in $xyxx$, the third interaction is orthogonal to the second. It is then reasonable to assume that given the same sample, a

pulse sequence with two $\frac{\pi}{2}$ rotations will select for a different sub-ensemble than one with only one $\frac{\pi}{2}$ rotation. The exact physical consequences of the differences between these signals merits further investigation.

3.2 Optical design of instrumentation

3.2.1 Production of Ultrafast Pulses

Ultrafast laser pulses are produced with Coherent Micra oscillator seeded Legend Elite regenerative amplifier. The output pulses of this system are centered at 800nm with a 30nm bandwidth and a 35fs temporal profile at a repetition rate of 5kHz. These pulses are then focused into a tube filled with argon gas for the nonlinear generation of broadband white light in the visible range. An example of the spectrum after white light generation is presented in Figure 3.2. An image of the white beam is presented in Figure 3.3. This light is then compressed to near the transform limit by using a combination of chirped mirrors and a BioPhotonics Inc. Femtojock multiphoton intrapulse interference phase scan (MIIPS) compression system.

3.2.2 Generation of Time Delays

The pulse is then split into the two arms of the spectrometer, pump and probe. An optical layout of the instrument is provided in Figure 3.4. The pump arm is sent down a retroreflective translation stage (Aerotech Inc.) and the NIREOS Gemini 2D delay stage to encode the waiting time (T) and coherence (τ) dimensions of the data, respectively. The Gemini 2D is a birefringent wedge delay system that is able to produce a collinear and phase-locked pulse pair from one input pulse [20]. A schematic of the Gemini 2D system, as shown in Figure 3.5, depicts how a time delay can be manipulated by projecting a pulse onto orthogonal axes of a trio of birefringent crystals. The input pulse is polarized at 45 degrees. It is then pro-

jected onto the orthogonal axes of the first crystal. This first crystal has its optical fast axis oriented at 0 degrees (y axis) meaning the component of the pulse projected onto the y axis will travel faster than the component on the x axis, creating a pulse pair. The next crystal is cut into a pair of wedges and has its optical fast axis at 90 degrees (x axis). This results in the opposite effect of the first block such that the x polarized components travel faster than the y polarized components. The time between these orthogonally polarized pulses can then be controlled with great precision by the thickness of the second crystal block. The third crystal has its fast axis along the direction of propagation (z axis) meaning that it has no effect on the time delay between the x and y polarized components. This block serves to maintain a constant dispersion over the measurement, as well as a constant time between pulses 2 and 3 (the waiting time) [20].

In the original design of the Gemini 2D, a polarizer was added to the end of the delay line to project the two pulses back onto the 45 degree axis to create a parallel pulse pair [20]. The version used in this experiment was specifically ordered with this polarizer omitted. The reason for this is that in order to measure the $yxxx$ and $xyxx$ tensors of the signal, one needs the first two pulses to be orthogonally polarized. Measuring these tensors of the chiral signal is often hindered by the polarization impurities introduced by standard polarizers and waveplates [19]. But, by modifying this instrument one can generate an orthogonal pulse pair with virtually no polarization impurities by taking advantage of the natural axes of a birefringent crystal.

3.2.3 Background-Free Detection

When measuring the $xxyx$ and $yyyx$ tensors of the chiral signal, one can utilize the fact that the signal is orthogonally polarized to the probe to create a background-free detection scheme. A version of this was designed by Ogilvie and coworkers [8] in order to reduce the often large probe background in a pump probe geometry 2DES setup. Briefly, the two pump

pulses were polarized at 45 degrees to the probe, and a polarizer was placed after the sample to remove most of the probe and measure the signal in a pseudo-background-free geometry. This way the amplitude of the probe self-hetererodyne could be controlled without affecting the probe power on the sample. Because some of the probe was allowed through for the heterodyne, some of the all parallel ($xxxx$) signal was still measured.

Our setup modifies that design for a chiral pulse sequence as well as the addition of a temporally separated local oscillator as shown in Figure 3.6. In the chiral probe sequences, $xxyx$ and $yyyx$, the probe is orthogonal to the signal allowing for background-free detection. In our case we want to completely remove the probe using a Wollaston Prism polarizer purchased from Thorlabs Inc. which has a 100,000:1 extinction ratio [21]. In the probe path before the sample, a thin crystal of /*alpha*-BBO purchased from Union Optic Inc. is placed such that the polarization of the probe is oriented slight off orthogonal to the optical fast axis. This allows most of the probe to be delayed about 1.3ps behind a small orthogonally polarized pulse which is used as a local oscillator. This local oscillator is then allowed to pass through the Wollaston prism polarizer with the chiral signal. The local oscillator then interferes with the signal on the camera allowing for retrieval of the signal phase, and therefore dispersive components of the signal, that is not typically possible in pump probe geometry 2DES. Additionally, when measuring the $yyyx$ component of the signal, all scatter from the pump and probe, as well as all transient absorption background should be removed by the Wollaston prism polarizer before the sample.

3.3 Data Acquisition Referencing Protocol

When acquiring data for the $yxxx$ and $xyxx$ pulse sequences, the data cannot be recorded in the background-free geometry as described above. This makes laser shot noise all the more important as a large probe background must be subtracted from each spectrum. Typically, in pump probe geometry 2DES, a chopper is used to block the pump arm every other laser

shot so that a background of probe only can be acquired. Then this probe only spectrum is subtracted from the pump-probe spectrum taken with the next laser shot. Therefore, any shot-to-shot fluctuations in the laser spectrum will result in subtraction errors introducing noise into the data. Single shot referencing has been often utilized in transient absorption spectroscopy to remove this shot correlated noise. In a paper by Dobryakov and coworkers [22], a single shot referencing protocol was developed for transient absorption spectroscopy which we have modified for 2DES. In our protocol a beam splitter is used to take a small portion of the probe before the sample and send it to a reference spectrometer, as shown in Figure 3.7. Then for each laser shot a reference spectrum of just the probe is recorded for the same laser shot that induces the signal. Each cycle then produced four spectra: reference pump on, data pump on, reference pump off, and data pump off. A schematic describing the basic program can be found in Figure 3.8. For each τ and T point, N cycles are recorded. Then for one pixel, p_i, at a time, the intensities on the reference and data cameras for the pump on (pump off) shots for all N cycles are plotted against each other and the slope of their least squares fit is recorded and called the quotient or q^* (q^0). The raw data is then saved as those two quotients as a function of camera pixel, τ and T. Then the processed data can be reconstructed using equation 3.6.

$$E_{sig} = \frac{q^* - q^0}{\sqrt{q^0}} \tag{3.6}$$

Because q^* contains the referenced signal-probe heterodyne as well as the probe intensity and q^0 contains just the referenced probe intensity, equation 3.6 isolates the signal electric field.

This referencing protocol compensates quite well for intensity fluctuations which are uniform across frequency. A potential issue arises that is not apparent in transient absorption due to the frequency correlated nature of 2DES. In the case of a cross peak, a spectral fluctuation that occurs at the excitation frequency will not be properly compensated for at

the detection frequency. This could potentially introduce additional noise or artifacts to the cross peaks. Fortunately, most shot-correlated noise is a uniform intensity fluctuation across frequency. A simple experiment correlating intensity fluctuations between random pixels can determine if this method is reasonable to apply. If the noise is found to be correlated across many different pixels, then this referencing protocol can be safely applied.

3.4 Data processing: scatter removal

The raw data acquired by the experiment is the intensity on the camera as a function of pixel, coherence time (τ), and waiting time (T). As the cameras are calibrated with atomic emission lamps filled with neon gas, a file is saved that maps camera pixel onto wavelength. In a typical 2DES experiment done in the pump-probe geometry, the intensity on the camera can be expressed in terms of all the electric fields which contribute, as shown in equation 3.7.

$$I_{cam} = |E_1 + E_2 + E_{pr} + E_{sig2D} + E_{sigPP1} + E_{sigPP2}|^2 \tag{3.7}$$

Where E_1 and E_2 are the two pump pulses, E_{pr} is the probe pulse, E_{sig2D} is the 2D signal, and E_{sigPP1} and E_{sigPP2} are pump probe signals generated by the two pump pulses.

3.4.1 Chiral Pump Sequences

This equation changes a little bit depending on which chiral signal we are measuring. We can utilize the fact that orthogonally polarized electric fields cannot interfere to remove some of the scatter contributions. Let's start with our chiral pump sequence $yxxx$. For this signal, there is no temporally separated LO so we can just expand equation 3.7 as is.

$$I_{cam} = E_1^2 + E_2^2 + E_{pr}^2 + E_{sig2D}^2 + E_{sigPP1}^2 + E_{sigPP2}^2 + E_1E_2 + E_1E_{pr} + E_1E_{sig2D} \quad (3.8)$$

$$+E_1E_{sigPP1} + E_1E_{sigPP2} + E_2E_{pr} + E_2E_{sig2D} + E_2E_{sigPP1} + E_2E_{sigPP2} + E_{pr}E_{sig2D}$$

$$+E_{pr}E_{sigPP1} + E_{pr}E_{sigPP2} + E_{sig2D}E_{sigPP1} + E_{sig2D}E_{sigPP2} + E_{sigPP1}E_{sigPP2} + C.C$$

In this equation the element we want to preserve while removing all others is $E_{pr}E_{sig2D}$ which is the signal heterodyne with the probe. The reason we want this and not the signal homodyne (E_{sig2D}^2) is that the heterodyne will be much stronger and still contains the information we want in the signal electric field. The first thing we notice is that a few of these signals go away due to the field configuration. For example, E_1E_2 cannot exist because E_1 and E_2 are orthogonally polarized and therefore cannot interfere. When we remove all similar terms, including those which will be removed by a polarizer after the sample oriented to only allow x polarized contributions, we obtain the equation:

$$I_{cam} = E_2^2 + E_{pr}^2 + E_{sig2D}^2 + E_{sigPP1}^2 + E_{sigPP2}^2 + E_2E_{pr} + E_2E_{sig2D} \quad (3.9)$$

$$+E_2E_{sigPP1} + E_2E_{sigPP2} + E_{pr}E_{sig2D} + E_{pr}E_{sigPP1} + E_{pr}E_{sigPP2}$$

$$+E_{sig2D}E_{sigPP1} + E_{sig2D}E_{sigPP2} + E_{sigPP1}E_{sigPP2} + C.C$$

We assume both of the pump-probe signal electric fields to be x polarized because those are the electric dipolar contributions and therefore the dominant signals.

The rest of these scatter contributions can be removed in a Fourier domain filtering method similar to Dalberg [23]. Each of these electric fields will behave differently from the

signal in at least one of the three domains of coherence frequency, waiting frequency and rephasing time and therefore can be removed by apodization of the signal.
Because the signal will oscillate in coherence time, due to the fact that it is in a coherence in this domain, we can remove all contributions that do not oscillate in this domain. The raw data can be Fourier transformed over the coherence time domain where a window can be applied that removes all contributions near the zero component in coherence frequency. Once this window is applied we are left with:

$$I_{cam} = E_{sig2D}^2 + E_2 E_{sig2D} + E_{pr} E_{sig2D} + E_{sig2D} E_{sigPP1} + E_{sig2D} E_{sigPP2} + C.C. \quad (3.10)$$

Similarly, the signal heterodyne should not oscillate in waiting time. Thus we can remove contributions that do oscillate in waiting time by Fourier transforming and apodizing around the zero component in frequency so all nonzero frequencies are removed. When we remove the terms in equation 3.10 that oscillate in waiting time we get equation 3.11.

$$I_{cam} = E_{sig2D}^2 + E_{pr} E_{sig2D} + E_{sig2D} E_{sigPP1} + E_{sig2D} E_{sigPP2} + C.C. \quad (3.11)$$

We can also remove terms that are far from zero in rephasing time. Because the probe is not temporally separated from the signal, the signal heterodyne should show up at time zero in rephasing time. Therefore, we can remove any contributions that are far from zero in rephasing time. It turns out that in this case, all of the terms that would be removed by this step have already been removed by other apodization steps. So, if we neglect the weak signal homodyne and heterodynes of signal fields we are left with our 2D signal homodyne as shown in equation 3.12.

$$I_{cam} = E_{pr} E_{sig2D} \quad (3.12)$$

3.4.2 Chiral Probe Sequences

The major difference between the scatter removal process for the chiral probe sequences is the replacement of the probe field, which is removed by a Wollaston prism polarizer before the camera, with a temporally separated LO field. We start with an equation very similar to Equation 3.7 but we have removed the probe field and added the LO field.

$$I_{cam} = |E_1 + E_2 + E_{LO} + E_{sig2D} + E_{sigPP1} + E_{sigPP2}|^2 \tag{3.13}$$

Now we can remove fields that don't interfere or survive a polarizer that removes anything not x polarized. For the $yyyx$ sequence this is trivial as all fields except the signal and LO are removed before the camera resulting in Equation 3.14 when the weak signal homodyne is neglected:

$$I_{cam} = E_{LO}E_{sig2D} \tag{3.14}$$

For the other chiral probe sequence ($xxyx$), the scatter contributions can be removed in the τ and T domains using the same methods described in the chiral probe sequences section. Scatter removal in rephasing time though is different because the signal heterodyne is no longer at zero time because the LO is now temporally separated from the signal. This gives us the additional ability of removing scatter which does not oscillate, or oscillates slowly in rephasing frequency. For example, in the $xxyx$ sequence, the E_1E_2 term cannot be removed via apodization in τ or T, but it can be removed in t because τ only needs to be scanned out to less than 100fs and so this interference will oscillate much slower than the signal heterodyne because the LO is separated from the signal by about 1200fs. Thus, temporally separating the LO allows for more robust scatter removal in the Fourier domain.

3.5 Conclusions

We have designed and built a dedicated spectrometer for the study of ultrafast chiral dynamics. The design of this instrument allows the more robust measurement of these often-neglected signals and their dynamics. By utilizing the natural polarization purity of birefringent crystals, we can achieve purely chiral signals with no achiral background. We can also achieve background-free detection in the pump probe geometry when selecting for chiral probe signals. Again by utilizing birefringent crystals we can create a temporally separated local oscillator to improve our signal strength and our scatter removal procedures. We have applied a single shot referencing technique, that when used correctly can compensate for laser shot correlated noise often found in pump-probe geometry experiments. All of these design elements together allow for Two-dimensional Circular Dichroism spectroscopy to give unprecedented insight into chiral electronic dynamics.

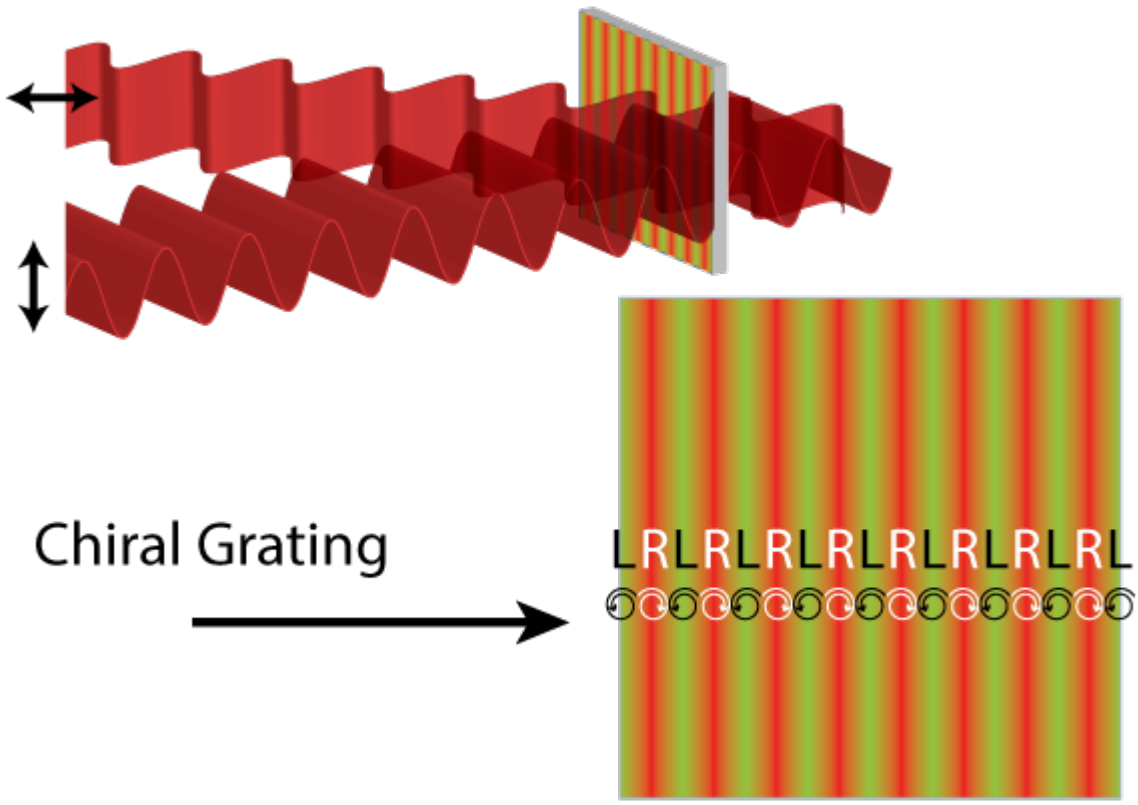

Figure 3.1: Depiction of a chiral grating. Orthogonally polarized fields crossing at an angle result in the sample experiencing a grating of LCP and RCP.

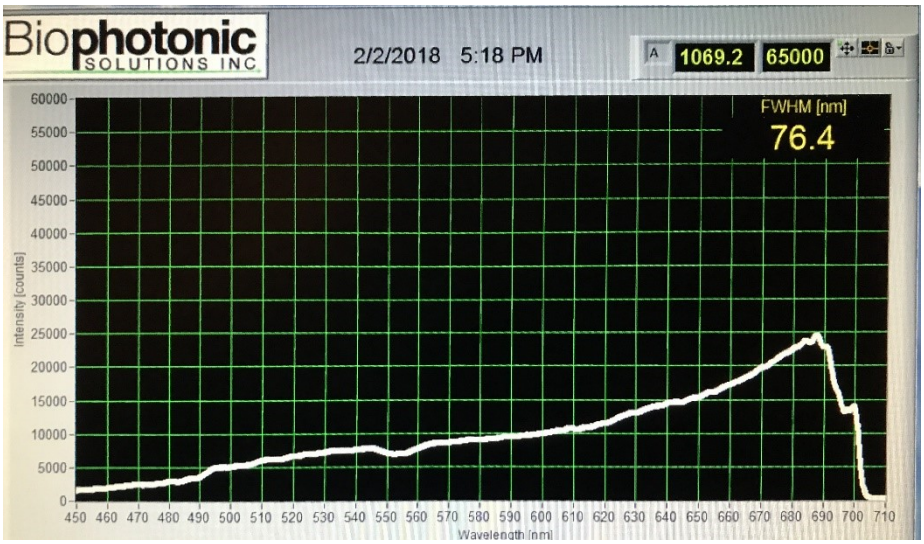

Figure 3.2: White light spectrum after self phase modulation in argon gas and filtering of the fundamental with a sputtered edge shortpass filter.

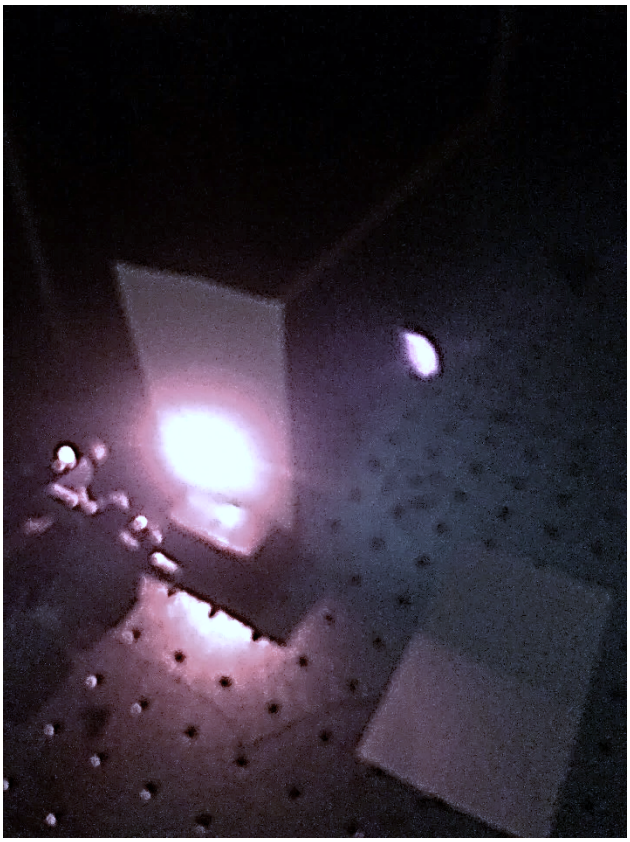

Figure 3.3: Image of broadband laser light after self phase modulation in argon gas.

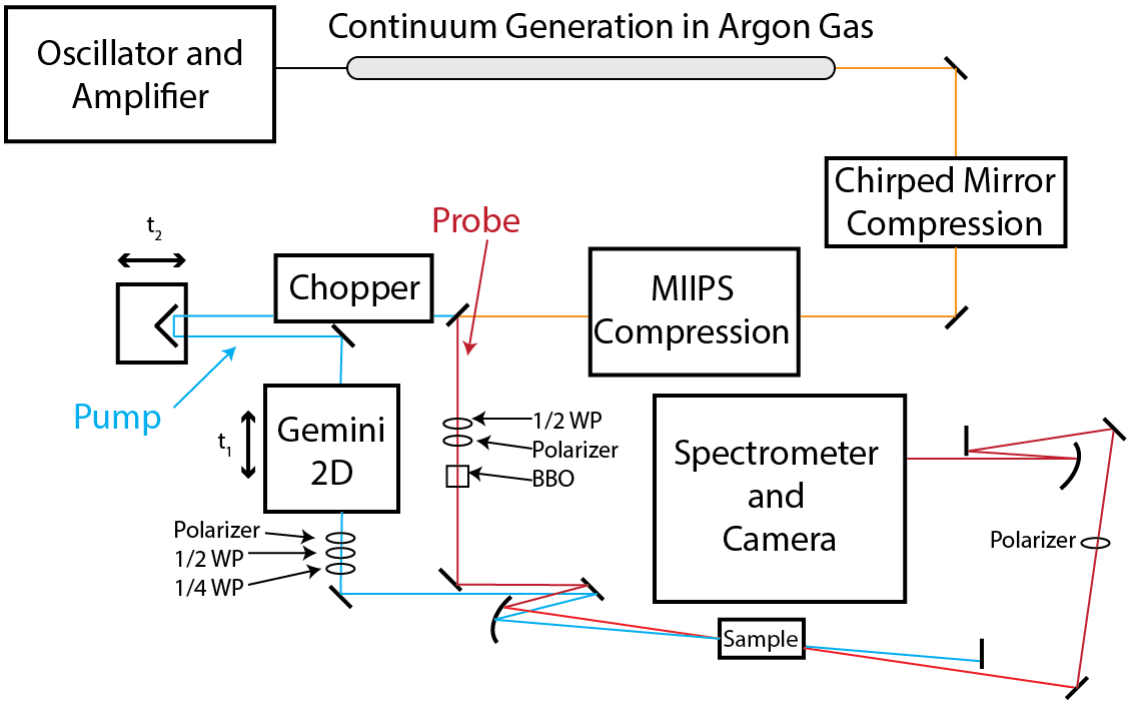

Figure 3.4: Optical layout of the two-dimensional circular dichroism instrument.

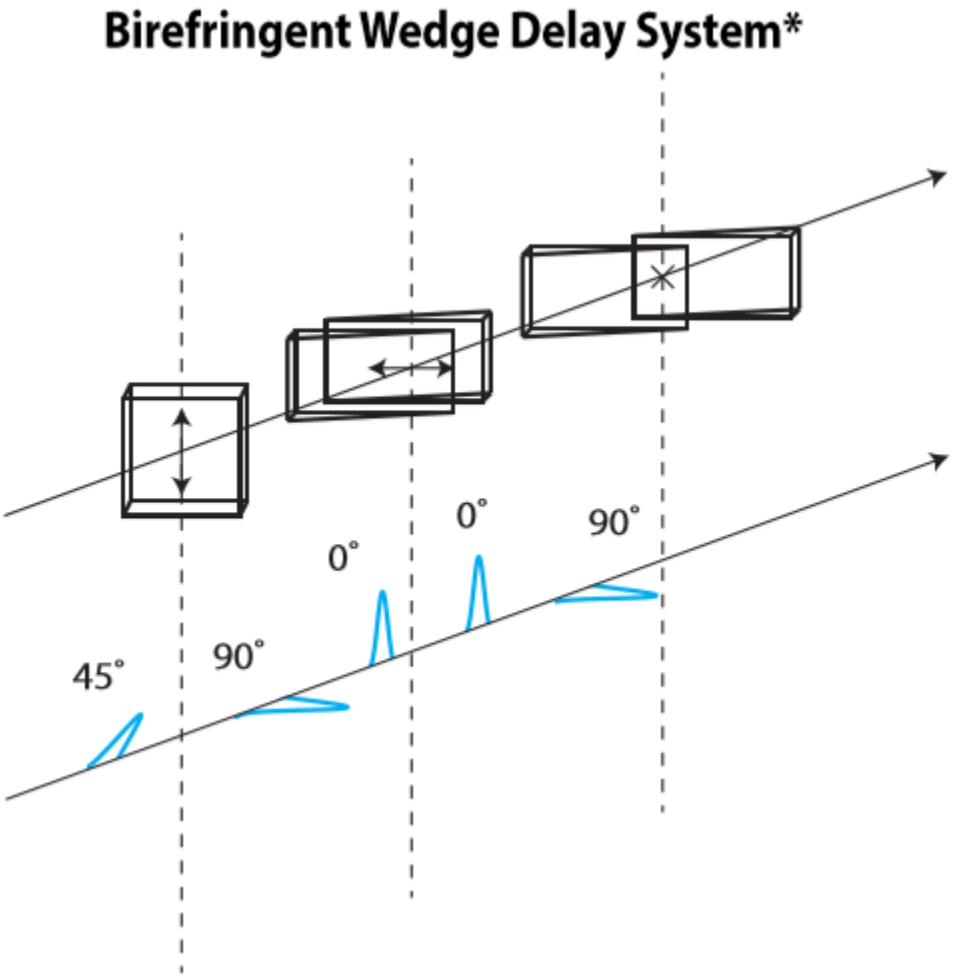

Figure 3.5: Depiction of birefringent wedge system utilized in NIREOS Gemini 2D. Arrows depict the optical fast axis of each crystal.

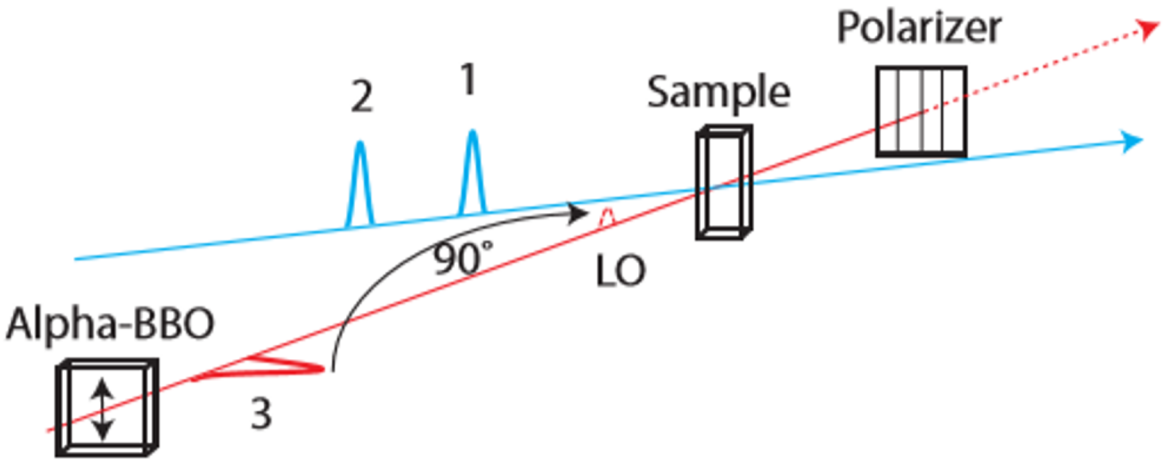

Figure 3.6: Detection scheme for background-free pump probe geometry two-dimensional spectroscopy with a temporally separated local oscillator. By placing a thin piece of birefringent material (α-BBO) in the probe path such that its optical fast axis is oriented a few degrees off of orthogonal to the probe polarization, most of the probe is delayed about 1.3ps but a small portion travels along the orthogonal optical fast axis. This creates a temporally separated, orthogonally polarized local oscillator.

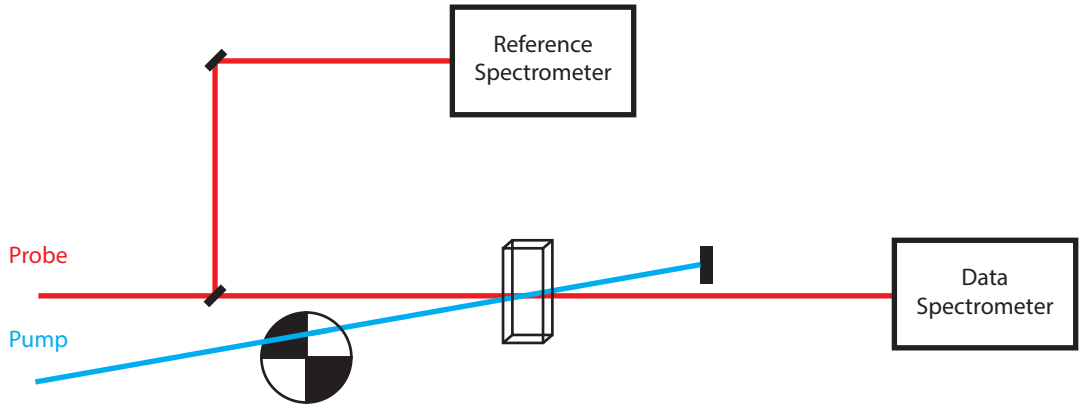

Figure 3.7: Optical setup of single shot referencing protocol. A portion of the probe is sent to a reference spectrometer with a beamsplitter before the sample in order to record shot-to-shot fluctuations in the laser light source.

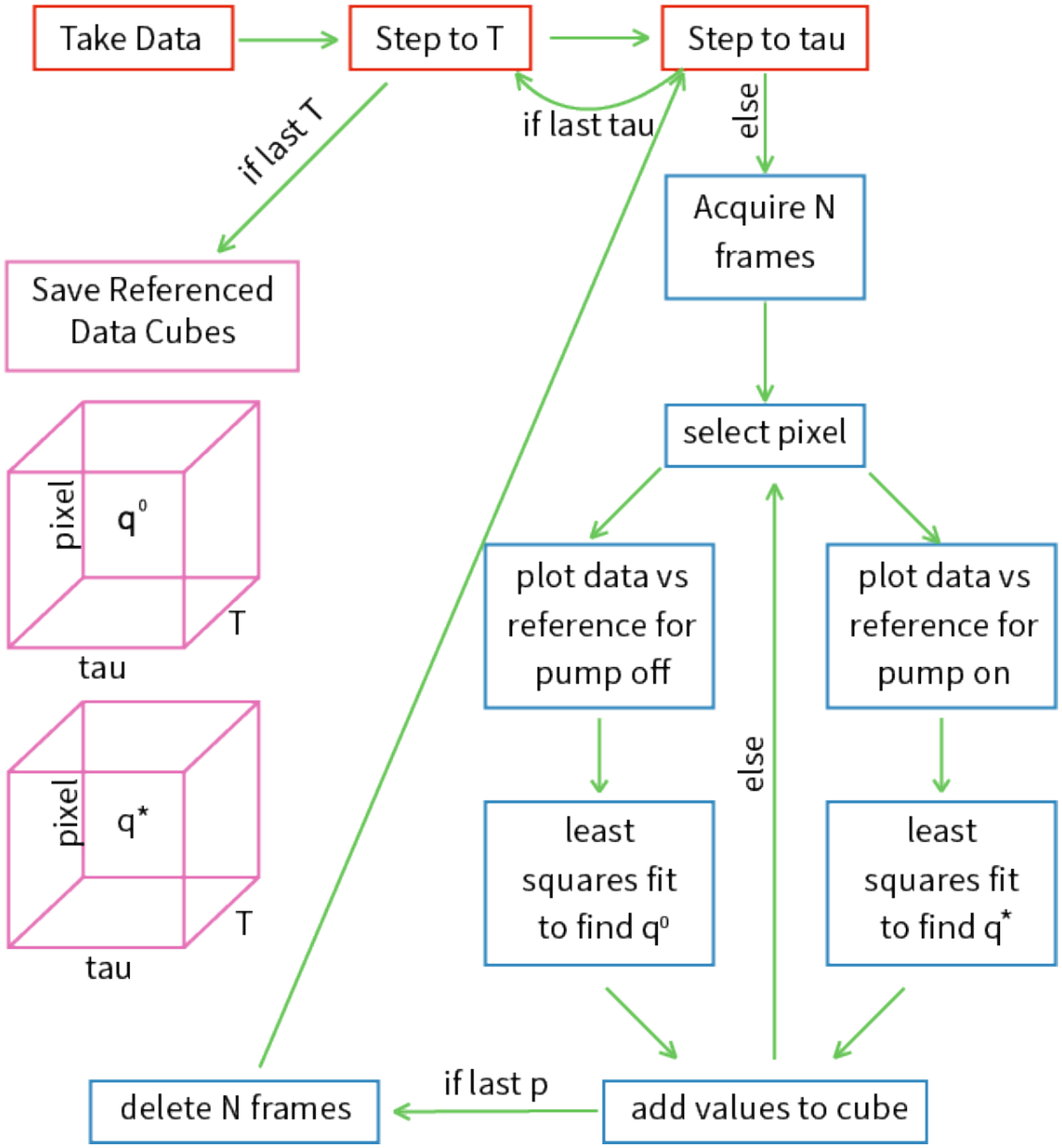

Figure 3.8: Simplified diagram describing the basics of the referencing protocol data acquisition program. Red boxes indicate the original data aquisition program, blue boxes indicated additions to incorporate the referencing protocol, and pink boxes are the referenced raw data.

REFERENCES

[1] Elad Harel, Andrew F Fidler, and Gregory S Engel. Real-time mapping of electronic structure with single-shot two-dimensional electronic spectroscopy. *Proceedings of the National Academy of Sciences*, 107(38):16444–16447, 2010.

[2] H. Zheng, J. R. Caram, P. D. Dahlberg, B. S. Rolczynski, S. Viswanathan, D. S. Dolzhnikov, A. Khadivi, D. V. Talapin, and G. S. Engel. Dispersion-free continuum two-dimensional electronic spectrometer. *Appl Opt*, 53(9):1909–17.

[3] Shaul Mukamel. *Principles of Nonlinear Optical Spectroscopy*. Oxford University Press, New York, 1995.

[4] Peter Hamm and Martin Zanni. *Concepts and Methods of 2D Infrared Spectroscopy*. Cambridge University Press, New York, 2011.

[5] Wei Xiong and Martin T Zanni. Signal enhancement and background cancellation in collinear two-dimensional spectroscopies. *Optics letters*, 33(12):1371–1373, 2008.

[6] Elizabeth L Read, Gregory S Engel, Tessa R Calhoun, Tomáš Mančal, Tae Kyu Ahn, Robert E Blankenship, and Graham R Fleming. Cross-peak-specific two-dimensional electronic spectroscopy. *Proceedings of the National Academy of Sciences*, 104(36):14203–14208, 2007.

[7] Martin T Zanni, Nien-Hui Ge, Yung Sam Kim, and Robin M Hochstrasser. Two-dimensional ir spectroscopy can be designed to eliminate the diagonal peaks and expose only the crosspeaks needed for structure determination. *Proceedings of the National Academy of Sciences*, 98(20):11265–11270, 2001.

[8] Franklin D Fuller, Daniel E Wilcox, and Jennifer P Ogilvie. Pulse shaping based two-dimensional electronic spectroscopy in a background free geometry. *Optics Express*, 22(1):1018–1027, 2014.

[9] Jens Dreyer, Andrew M. Moran, and Shaul Mukamel. Tensor components in three pulse vibrational echoes of a rigid dipeptide. *Bull. Korean Chem. Soc.*, 24(8):1091–1096, 2003.

[10] D. Abramavicius and S. Mukamel. Coherent third-order spectroscopic probes of molecular chirality. *J Chem Phys*, 122(13):134305.

[11] A. F. Fidler, V. P. Singh, P. D. Long, P. D. Dahlberg, and G. S. Engel. Dynamic localization of electronic excitation in photosynthetic complexes revealed with chiral two-dimensional spectroscopy. *Nat Commun*, 5:3286.

[12] Darius Abramavicius and Shaul Mukamel. Chirality-induced signals in coherent multidimensional spectroscopy of excitons. *The Journal of chemical physics*, 124(3):034113, 2006.

[13] D. I. Holdaway, E. Collini, and A. Olaya-Castro. Isolating the chiral contribution in optical two-dimensional chiral spectroscopy using linearly polarized light. *Opt Express*, 25(6):6383–6401.

[14] Darius Abramavicius, Wei Zhuang, and Shaul Mukamel. Probing molecular chirality via excitonic nonlinear response. *Journal of Physics B: Atomic, Molecular and Optical Physics*, 39(24):5051–5066, 2006.

[15] D. L . Andrews and T. Thirunamachandran. On three-dimensional rotational averages. *J Chem Phys*, 67:5026.

[16] David W Neyer, Larry A Rahn, David W Chandler, Jon A Nunes, and William G Tong. Circular dichroism spectroscopy using coherent laser-induced thermal gratings. *Journal of the American Chemical Society*, 119(35):8293–8300, 1997.

[17] John T Fourkas, Rick Trebino, and MD Fayer. The grating decomposition method: A new approach for understanding polarization-selective transient grating experiments. i. theory. *The Journal of chemical physics*, 97(1):69–77, 1992.

[18] Masahide Terazima. A new method for circular dichroism detection using cross-polarized transient grating. *The Journal of Physical Chemistry*, 99(7):1834–1836, 1995.

[19] Jun-Ho Choi, Sangheon Cheon, Hochan Lee, and Minhaeng Cho. Two-dimensional nonlinear optical activity spectroscopy of coupled multi-chromophore system. *Physical Chemistry Chemical Physics*, 10(26):3839–3856, 2008.

[20] Daniele Brida, Christian Manzoni, and Giulio Cerullo. Phase-locked pulses for two-dimensional spectroscopy by a birefringent delay line. *Opt. Lett.*, 37(15):3027–3029, 2012.

[21] Thorlabs Inc. Wollaston prisms, 2022.

[22] A. L. Dobryakov, S. A. Kovalenko, A. Weigel, J. L. Perez-Lustres, J. Lange, A. Muller, and N. P. Ernsting. Femtosecond pump/supercontinuum-probe spectroscopy: Optimized setup and signal analysis for single-shot spectral referencing. *Rev. Sci. Instrum.*, 81(11):113106.

[23] Peter Dahlberg. *Energy Transfer Events In Photosynthesis Observed In Vivo Using Non-linear Ultrafast Spectroscopies*. Thesis, 2016.

CHAPTER 4

TWO-DIMENSIONAL ELECTRONIC SPECTROSCOPY IN THE PUMP-PROBE GEOMETRY WITH A TEMPORALLY SEPARATED LOCAL OSCILLATOR

Advances in ultrafast spectroscopy have been paramount to understanding dynamical systems in the past several decades [1–5]. The ability to resolve both frequency and time allow for mapping of energy transfer pathways [6], as well as unique observation of spectral broadening mechanisms [7]. The pump-probe geometry provides an opportunity to develop simple and robust instrumentation for the acquisition of 2DES spectra [1, 2, 8–11].

4.1 Methods

Two-dimensional Fourier transform spectroscopy (2DFT) consists of three ultrafast, broadband pulses interacting with a sample to produce a third-order polarization which generates a signal that can be imaged on a camera [12]. The three pulses and the signal naturally define three time domains, the first and third of which can be Fourier transformed to produce a frequency-frequency correlation map. The second time domain is typically used to provide the dynamical information about the system. The signal is generated in a phase-matched direction which is determined by the wavevectors of the excitation pulses [13]. Typically, the two main geometries used are the pump-probe geometry and the BOXCARS geometry. In the pump-probe geometry the first two interactions are collinear and the third pulse, or the probe, enters the sample at a small angle relative to the pump beam. The resulting signal must then travel collinearly with the probe. This geometry results in a very phase stable measurement but with a large background from the probe. The BOXCARS geometry, on the other hand, has the three excitation pulses entering the sample at different angles, resulting in the signal traveling in a unique phase-matched direction. In this geometry, the signal can

be detected background-free, and an independent local oscillator can be added to heterodyne with the signal on the camera. The downside to BOXCARS is the fact that because the excitation pulses must all travel different paths, their phase relationship becomes unknown and an additional experiment must be done to recover that phase information [14].

Advances in pump-probe geometry 2DFT have resulted in pseudo-background-free spectrometers published by Ogilvie and coworkers [1, 2] and Zanni and coworkers [15]. This approach reduces the background by detecting some electric dipolar signals in which the signal is orthogonally polarized to the probe field such that a polarizer can be used to remove most of the probe field. In their experiments, some of the probe field is allowed in to the detector in order to heterodyne with the signal in a tunable way. Our approach utilizes a $\frac{\pi}{4}$ $\frac{\pi}{4}$ $\frac{\pi}{4}$ 0 polarized pulse sequence, but introduces a fourth pulse (the local oscillator) which is orthogonally polarized to the probe field and about 1.3 ps ahead of the probe in time. This temporal delay allows for larger interferometric fringe contrast at the detector than simply self-heterodyning with the probe field.

The LO is generated by placing a thin alpha-BBO crystal in the probe path, oriented such that the optical fast axis is a tilted a few degrees off normal from the probe polarization. This results in a small portion of the probe being projected onto the fast axis of the crystal, creating our local oscillator. The probe field is then completely removed by the polarizer after the sample, leaving only the signal and local oscillator to interfere on the detector. Thus, the instrument described here is able to utilize the phase stable nature of the pump-probe geometry while maintaining the background-free and temporal heterodyning capabilities of BOXCARS. One must take additional care when interpreting these spectra as the tensors of the signal being measured are $xyxy + yxxy$. This requires more subtle interpretation but the suppression and enhancement of different pathways can be determined by calculating the orientational factors for these tensors, if the angles between the transition dipoles are known [16].

4.1.1 Correcting for Phase Acquired During the Measurement

Though using a local oscillator has many benefits, as described above, the one problem is that now there is an additional phase evolved between the signal and the LO which is described by equation 4.1 [17].

$$S(t_1, t_2, t_3) \propto e^{-i\phi_{LO}} \sum_n iR_n(t_1, t_2, t_3) \tag{4.1}$$

where ϕ_{LO} is the phase acquired during t_{LO}.

Fortunately, we are imaging the interferogram produced between the LO and the signal on the camera and can extract the phase from that through a Fourier transform [12, 17]. If that phase is known we can add it back in such that the $e^{-i\phi}$ term goes to zero and the signal is once again proportional to the material response. The real portion of that complex signal gives us back the purely absorptive lineshapes [17].

There is also additional phase acquired during t_1 that results from the dispersion mismatch in the birefringent delay line [18]. This phase is a function of the delay time as described by equation 4.2

$$\Delta\phi = \omega_0 \left[\left(\frac{1}{v_{go}} - \frac{1}{v_p} \right) - \left(\frac{1}{v_{ge}} - \frac{1}{v_p} \right) \right] \Delta t_1 / \left(\frac{1}{v_{ge}} - \frac{1}{v_{go}} \right) \tag{4.2}$$

where ω_0 is the carrier frequency, v_{ge} and v_{go} are the group velocities for the extraordinary and ordinary axes, respectfully, and v_p is the phase velocity at the carrier frequency [18].

This phase can be either calculated by equation 4.2 or measured interferometrically by imaging E_1E_2 scatter on the camera and recording the phase as a function of t_1.

4.2 Conclusions

We have described here a novel approach to two-dimensional optical spectroscopy in the pump-probe geometry. This instrument successfully combines the background-free and tem-

poral heterodyning capabilities of BOXCARS 2DES with the phase stability and robustness of pump-probe geometry 2DES. This instrument should open the door for the consistent and rapid collection of purely absorptive spectra.

REFERENCES

[1] Jeffrey A Myers, Kristin LM Lewis, Patrick F Tekavec, and Jennifer P Ogilvie. Two-color two-dimensional fourier transform electronic spectroscopy with a pulse-shaper. *Optics express*, 16(22):17420–17428, 2008.

[2] Franklin D Fuller, Daniel E Wilcox, and Jennifer P Ogilvie. Pulse shaping based two-dimensional electronic spectroscopy in a background free geometry. *Optics Express*, 22(1):1018–1027, 2014.

[3] H. Zheng, J. R. Caram, P. D. Dahlberg, B. S. Rolczynski, S. Viswanathan, D. S. Dolzhnikov, A. Khadivi, D. V. Talapin, and G. S. Engel. Dispersion-free continuum two-dimensional electronic spectrometer. *Appl Opt*, 53(9):1909–17.

[4] Elad Harel, Andrew F Fidler, and Gregory S Engel. Real-time mapping of electronic structure with single-shot two-dimensional electronic spectroscopy. *Proceedings of the National Academy of Sciences*, 107(38):16444–16447, 2010.

[5] David M Jonas. Two-dimensional femtosecond spectroscopy. *Annual review of physical chemistry*, 54(1):425–463, 2003.

[6] Jacob S Higgins, Lawson T Lloyd, Sara H Sohail, Marco A Allodi, John P Otto, Rafael G Saer, Ryan E Wood, Sara C Massey, Po-Chieh Ting, Robert E Blankenship, et al. Photosynthesis tunes quantum-mechanical mixing of electronic and vibrational states to steer exciton energy transfer. *Proceedings of the National Academy of Sciences*, 118(11), 2021.

[7] Eric M Janke, Nicholas E Williams, Chunxing She, Danylo Zherebetskyy, Margaret H Hudson, Lili Wang, David J Gosztola, Richard D Schaller, Byeongdu Lee, Chengjun Sun, et al. Origin of broad emission spectra in inp quantum dots: Contributions

from structural and electronic disorder. *Journal of the American Chemical Society*, 140(46):15791–15803, 2018.

[8] Martin T Zanni, Nien-Hui Ge, Yung Sam Kim, and Robin M Hochstrasser. Two-dimensional ir spectroscopy can be designed to eliminate the diagonal peaks and expose only the crosspeaks needed for structure determination. *Proceedings of the National Academy of Sciences*, 98(20):11265–11270, 2001.

[9] Patrick F Tekavec, Jeffrey A Myers, Kristin LM Lewis, and Jennifer P Ogilvie. Two-dimensional electronic spectroscopy with a continuum probe. *Optics letters*, 34(9):1390–1392, 2009.

[10] Weida Zhu, Rui Wang, Chunfeng Zhang, Guodong Wang, Yunlong Liu, Wei Zhao, Xingcan Dai, Xiaoyong Wang, Giulio Cerullo, Steven Cundiff, et al. Broadband two-dimensional electronic spectroscopy in an actively phase stabilized pump-probe configuration. *Optics Express*, 25(18):21115–21126, 2017.

[11] Julien Réhault, Margherita Maiuri, Aurelio Oriana, and Giulio Cerullo. Two-dimensional electronic spectroscopy with birefringent wedges. *Review of Scientific Instruments*, 85(12):123107, 2014.

[12] Shaul Mukamel. *Principles of Nonlinear Optical Spectroscopy*. Oxford University Press, New York, 1995.

[13] Andrei Tokmakoff. Time dependent quantum mechanics and spectroscopy, 2014.

[14] John D Hybl, Allison Albrecht Ferro, and David M Jonas. Two-dimensional fourier transform electronic spectroscopy. *The Journal of Chemical Physics*, 115(14):6606–6622, 2001.

[15] Wei Xiong and Martin T Zanni. Signal enhancement and background cancellation in collinear two-dimensional spectroscopies. *Optics letters*, 33(12):1371–1373, 2008.

[16] Jens Dreyer, Andrew M. Moran, and Shaul Mukamel. Tensor components in three pulse vibrational echoes of a rigid dipeptide. *Bull. Korean Chem. Soc.*, 24(8):1091–1096, 2003.

[17] Peter Hamm and Martin Zanni. *Concepts and Methods of 2D Infrared Spectroscopy*. Cambridge University Press, New York, 2011.

[18] Daniele Brida, Christian Manzoni, and Giulio Cerullo. Phase-locked pulses for two-dimensional spectroscopy by a birefringent delay line. *Opt. Lett.*, 37(15):3027–3029, 2012.

CHAPTER 5

LEVERAGING DYNAMICAL SYMMETRIES IN TWO-DIMENSIONAL ELECTRONIC SPECTRA TO EXTRACT POPULATION TRANSFER PATHWAYS

*This chapter is adapted from Reference [1]. My primary contribution was section 5.3.2.

Two-dimensional electronic spectroscopy (2DES) is a technique used extensively over the last two decades to study the excited state behavior of condensed phase systems [2–5]. It has been used to study excited state dynamics in photosynthetic light harvesting complexes [6–12], photobiological systems such as rhodopsin proteins [13, 14], synthetic molecular systems [15–18], and materials systems [19, 20]. In 2DES, the electronic excitation energies of a system are correlated with the detection energies, revealing how the excited states are coupled [21, 22]. This coupling can be tracked through the waiting time with femtosecond precision to monitor the dynamics of processes such as exciton energy transfer (EET). 2DES is a versatile tool to unpack many aspects of excited state system and bath interactions in molecular systems, as one can study spectral lineshapes [23–25], coherence dynamics [4, 5], and population kinetics [26, 27] in the signal analysis. Due to the overlap of multiple peaks and dynamic contributions to 2DES signals, it remains difficult to extract the exact kinetic rates that govern energy transfer [27, 28]. The illumination of a sample with an ultrafast laser source excites many different dynamical subensembles within the system [21, 29]. These dynamics can converge onto a single lineshape when the excitation and detection energies of the subensembles are similar, and many of these lineshapes overlap at finite temperatures. The waiting time evolution at any given point on a 2D spectrum is thus generated from many types of electronic or nuclear motion, such as EET, ground state recovery, coherence, spectral diffusion, and vibrational relaxation [30]. It has been shown that 2D spectroscopy is capable of resolving the entire energy transfer matrix of spectrally

resolved complexes [28], and previous reports have extracted population transfer tables in 2D spectra with global fitting analyses [7] and by using a combination of decay associated and coherence associated spectra [31]. In this paper, we extend an analysis method to fit to the kinetic parameters for population transfer in two-dimensional spectra. This method has been used to differentiate the kinetics of excitonic pathways in photosynthetic light harvesting systems [32], but it can in principle be exported to other systems. The paper is outlined as follows. In Section 5.1, we describe the theory of nonlinear spectroscopy and how Feynman pathways allow one to calculate the relative probability that dynamical subensembles contribute to the signal. We then enumerate the types of Feynman pathways in excitonic systems and their relative signal strengths, spectral location, and time evolution. We describe signal processing steps to extract time constant information and methods to improve the accuracy. In Section 5.2, we test the method's accuracy using simulated two-dimensional electronic spectra in a diverse set of systems with increasing complexity and find that the method is robust to molecular complexes with dark states and interfering resonant vibrations. In Section 5.3, we discuss how the analysis method can be applied to other spectroscopic experiments such as materials systems and chiral pulse polarization sequences. We discuss the behavior of these systems and illustrate how Feynman pathways can more rigorously describe their dynamics.

5.1 Theory and Analysis Method

5.1.1 Molecular Response Functions and Their Time Evolution

In 2DES, the nonlinear signal is generated in response to three pulses acting on the system [21, 29]. The pulses coherently couple the molecular dipoles and generate the third order polarization:

$$P^{(3)}(t,t_1,t_2,t_3) = \int dt_1 \int dt_2 \int dt_3 E_3(t-t_3)\cdot \tag{5.1}$$

$$E_2(t - t_3 - t_2)E_1(t - t_3 - t_2 - t_1)R^{(3)}(t_1, t_2, t_3)$$

The polarization is dependent on three time variables representing the time delay between each pulse, referred to as the coherence time t_1, the waiting time t_2, and the rephasing time t_3. In our semiclassical formalism, the three pulses are treated classically, and the quantum mechanical information of the molecular system is encapsulated in the third order response function $R^{(3)}$:

$$R^{(3)}(t_1, t_2, t_3) = -\left(-\frac{i}{\hbar}\right)^3 \langle \mu(t_3 + t_2 + t_1)[(t_2 + t_1), [\mu(t_1), [\mu(0), \rho(-\infty)]]]\rangle \tag{5.2}$$

The response function describes how the ensemble of states reacts to the dipole perturbation induced by the laser pulses [33]. The molecular density matrix ρ is acted on by the dipole operator μ [22]. The nested commutators allow all possible combinations of dipole operators to act on either side of the density matrix, and the brackets $\langle\ \rangle$ depict an average over the entire thermal ensemble. The magnitude of the transition dipole moment terms $\mu_{ij} = \langle\psi_i|\mu|\psi_j\rangle$ determine the relative probability of transitioning between states i and j [34]. With multiple dipole interactions acting on the density matrix, many permutations given by the nested commutators, and averaging over the thermal ensemble, there is a large number of summed terms in the total third order response function. The terms scale rapidly with the number of dipole-accessible electronic, vibrational, and vibronic states in the system. Each term in the response function describes a particular subensemble that evolves in response to the laser pulses. Each of these subensembles has a probability of contributing to the signal depending on multiple intrinsic properties of the system, such as the transition dipole moments and the transfer rate between the states coupled to the subensemble population.

In this analysis, we use double-sided Feynman pathways to visualize and track the components of the third order response function (Equation 5.2) [22, 29, 35]. Feynman pathways

have been used in many types of physical systems to visualize the perturbative behavior of many body systems [6]. An example Feynman pathway that undergoes waiting time dynamics is shown in Figure 5.1. The diagonal lines represent pulses driving transitions on either the bra or ket side of the density matrix. Over each time interval, the signal evolves as either a coherence or a population. For coherences, the signal oscillates with a frequency given by the energy difference between the two states and decays with a dephasing time τ_{deph}:

$$G(t) \propto e^{i\omega_{ij}t - t/\tau_{deph}} \tag{5.3}$$

Here, $G(t)$ is the Green's function operator that drives time evolution to time t, and $\omega_{ij} = (E_i - E_j)/\hbar$ [21, 22]. The coherence generated in the third time interval produces the signal, which we represent with the dashed line. For populations, the signal strength is proportional to the population of the subensemble at time t [35]. As such, the signal will increase or decrease with the microscopic population dynamics in the system. For example, the pathway shown in Figure 5.1 undergoes population dynamics during the waiting time t_2. Excitation energy transfers from the excitonic state a to state b with a phenomenological time constant τ_{ab}, as shown in the simplified two excited state system adjacent to the Feynman pathway. The signal during t_2 that evolves from this pathway, shown to the right, is directly proportional to the population of exciton b that accumulates due to energy transfer from exciton a. The signal strength is weighted by the transition dipole moments for each laser interaction (in this case $|\mu_a|^2|\mu_b|^2$, shown as the signal peak).

The population dynamics during the waiting time t_2 and how the dynamics of all possible Feynman pathway contribute to the overall signal are the principle concern of this analysis. We consider each Feynman pathway to represent a particular dynamical subensemble of the system. Each pathway carries its own waiting time kinetics due to the microscopic behavior of the system. Its relative contribution to the total signal is determined by the dephasing times of the coherences, the kinetics of the populations (typically during the waiting time),

and the transition dipole amplitude from the four light-matter interactions. The 24 possible pathways for a two excited state system with a shared ground state constitute a basis set that can be used to describe the total response of a larger set of states, including vibrational energy levels.

5.1.2 Time Constant Extraction Method

There are symmetries in the dynamical evolution of diagonal and below diagonal cross peaks of 2D spectra that we can exploit to isolate the time constants for energy transfer. The strongest signals in the diagonal and below diagonal peaks corresponding to the exciton energies are the ground state bleach (GSB) and stimulated emission (SE) signals. The goal of this analysis is to remove the contribution of the GSB signals to the waiting time evolution of these peaks. Doing so isolates the SE signals, which evolve through the waiting time exclusively from interexcitonic dynamics. These signals can thus be fit exactly to kinetic equations to isolate the phenomenological time constants for energy transfer. The following section describes the Feynman pathways (Figure 5.2), approximations, and steps that this method entails. We first make the approximation to ignore the relative contribution of coherence and excited state absorption pathways to the diagonal and below diagonal waiting signals (see Figure 5.2C-D). The excited state absorption pathways can be neglected because 1) the relative transition dipole strengths from excited state absorption (μ_{fe}) are smaller than between the ground and first excited state (μ_{eg}), 2) lifetime broadening of the short-lived coherence in the rephasing time causes the signal to spread over a broader area on the detection axis, which reduces the pathway's relative contribution to each point in the detection axis [33, 36], and 3) their position on the spectrum and thus overlap with relevant peaks depends on the specific system and its intrinsic properties such as exciton binding energy. The relative weakness of ESA signals can be seen in the largely positive diagonal and below-diagonal 2DES signals of photosynthetic light harvesting complexes [7, 9, 26, 37, 38],

demonstrating that the positive SE and GSB pathways produce stronger signals in these regions. For coherence pathways, the exponential decay of coherences due to dephasing will be symmetric about zero and therefore not contribute to the overall monotonic curvature of the signals due to energy transfer. Therefore, the monotonic curvature of the signals should be primarily due to population dynamics. We will test these two approximations and assess their accuracy in the following section.

The Feynman pathways that contribute the most signal strength and waiting time signal change in diagonal and below-diagonal regions are the GSB, GSB recovery pathways, and population SE pathways. Figure 5.2A-B shows these three pathways and their subsequent waiting time evolution for a mock exciton e_a diagonal peak and exciton $e_a - e_b$ below diagonal cross peak. For the stimulated emission pathways, the waiting time dynamics evolve differently between diagonal and below diagonal peaks. The diagonal pathway decays with waiting time due to loss of exciton e_a population as it transfers to exciton e_b, the ground state, or to other states in the system. The cross peak pathway increases with waiting time as $e_a - e_b$ energy transfer occurs but then will decrease as the population subsequently leaves exciton e_b. At both the e_a diagonal and $e_a - e_b$ cross peak, the ground state bleach and bleach recovery pathways undergo the same time evolution in the waiting time with a time constant given by the relaxation from exciton a to the ground state. The only difference between the bleach signals of each region is the interaction of the third pulse. The diagonal pathway produces a $|e_a\rangle\langle g|$ coherence while the cross peak pathway produces a $|e_b\rangle\langle g|$ coherence. We take advantage of the symmetry of the bleach pathways to remove their contribution to the signal evolution. At each peak, the three pathways scale with the same transition dipole strength, but the strength is different between peaks. We correct for this difference by first normalizing each signal:

$$norm(Sig(T)) = \frac{Sig(T) - Sig(T_i)}{|Sig(T_f) - Sig(T_i)|} \tag{5.4}$$

Here, T_i and T_f are the initial and final waiting times for each time interval. The normalization step removes the amplitude differences between the diagonal and cross peaks but keeps the difference curvature due exponential decay rates. We can subtract the normalized diagonal signal from its corresponding normalized lower diagonal cross peak signal to approximately remove the bleach contribution and maintain the stimulated emission pathway kinetics. The time evolution of this signal is purely due to energy transfer between excited state populations (Figure 5.2E), so the time constant for the subtracted signal is a parameter that can be used to fit to energy transfer time constants. The schematic of steps for isolating the kinetic rate constants is shown in Figure 5.3. For clarity, we use sequential exciton numbering, where exciton 1 is the lowest energy. First, diagonal and cross peak regions of the excitonic peaks are averaged using circular windows. Averaging over finite regions removes the bath dynamics from the signal such as vibrational relaxation and spectral diffusion. These dynamics affect the lineshape evolution in the spectra, and averaging removes this effect so that the signal evolves in time exclusively from excitonic dynamics. Then, a waiting time interval is selected for curve fitting, typically from early waiting times between 50 and 100 fs to about half the experimental time, typically 1000 fs. The time constant fitting procedure is then performed starting with energy transfer between the lowest two excitonic states. The 2 diagonal and 2-1 cross peak are normalized according to Equation 5.4 and then subtracted from one another. If necessary, the τ_{1L} time constant can be obtained from the exciton 1 diagonal. Because the bleach recovery signal is removed in the subtraction and the stimulated emission signals exclusively evolve on the short time scale due to energy transfer between excitons 2 and 1 (see above), the fit time constant for the subtracted signal must be the energy transfer time constant τ_{21}.

The procedure then moves to the next highest excitonic state. The time constant τ_{3L} ('3 loss,' or transfer from exciton 3 to other states) is estimated as the short time constant in

a biexponential fit to the 3 diagonal. The τ_{3L} value must satisfy the other energy transfer time constants $\tau 32$ and τ_{31} according to $k_{3L} = \frac{1}{\tau_{3L}} = \frac{1}{\tau_{31}} + \frac{1}{\tau_{32}}$. The 3 diagonal and below diagonal cross peaks are then normalized, and one cross peak is selected to be subtracted from the diagonal. Typically, the 3-1 cross peak is chosen to ensure a good fit to the subtracted time constant because it monotonically increases over short experimental times, while the 3-2 cross peak often has flatter curvature because of energy transfer in and out of exciton 2. The normalized diagonal and cross peak signals are subtracted from one another, and the remaining signal is fit to a monoexponential decay function. Solutions to differential equations for energy transfer are then numerically calculated to fit to the diagonal and cross peak stimulated emission signals. The numerically calculated signals are normalized, subtracted, and fit to a monoexponential decay, and the resulting time constant value is compared to the experimental data. The calculation is repeated for all short time values of τ_{31} and τ_{32} under the constraint of τ_{3L}, and the combination that best matches the experimental subtracted time constant is selected as the best fit for energy transfer. We should note that it is necessary to first calculate τ_{21} because it is used as a parameter in the differential equation. The numerical fitting procedure is repeated for higher energy levels as necessary. The entire analysis, starting from the normalization of the 2 diagonal and 2-1 cross peak, is then repeated using different time intervals until the time interval spans the entire experimental time, typically 2000 fs. For each time interval, the goodness of fit for the numerical signals is evaluated by calculating the root-mean-squared difference between the subtracted 2D signals and the numerically calculated subtracted signals. Typically, there is a range of time intervals that best fits the subtracted signals. The time constants over the best fitting time intervals are averaged over this best fitting interval to result in the final time constant values for EET. This final averaging step minimizes error due to arbitrary choice of time interval. We demonstrate this process with data from the Fenna-Matthews-Olson (FMO) complex from green sulfur bacteria in reducing conditions. This analysis has been

conducted in a previous study without the final waiting time interval average [32]. Figure 5.4A shows a two-dimensional spectrum of FMO at waiting time 800 fs. The three diagonal peaks represent excitons 4, 2, and 1, which constitute a major energy transfer pathway through the complex [26]. The time traces are averaged using a 70 cm^{-1} circular window. Figure 5.4B-E depicts the signal subtraction process using a waiting time window range from 100 to 2000 fs. Figure 5.4B is the monoexponential fit to the normalized 2 diagonal subtracted from the normalized 2-1 cross peak, which isolates the τ_{21} time constant. Figure 5.4C is the fit to the averaged exciton 4 diagonal peak, where the short time constant τ_1 =225 fs is estimated as the exciton 4 loss time constant. The monoexponential fit to the normalized 4 diagonal subtracted from the normalized 4-1 cross peak (Figure 5.4D) is then reproduced in the numerical simulation (Figure 5.4E) such that τ_{41} and τ_{42} satisfy the τ_{4L} constraint. After repeating this process over waiting time end points from 600 to 2000 fs, we find that the lowest root-mean-square error falls in the range from 1700 to 2000 fs (Figure 5.4F). After averaging over this range, we obtain the final averaged time constants τ_{21ave} =453 fs, τ_{42ave} =409 fs, and τ_{41ave} =496 fs.

5.2 Results

5.2.1 Global Response and Method Accuracy for Excitonic Systems

We simulated two-dimensional spectra of multi state systems by calculating each component of the total response in the time domain, following the procedure laid out in Ref. [29]. We used all combinations of Feynman pathways from a system with two excited states (Figure S1) to form a basis set to model systems with multiple excited states, taking care not to double count pathways. We then Fourier transformed the t_1 and t_3 axes of the total response to obtain ω_1 and ω_3. We simulated three classes of energy transfer systems, shown in Figure 5.5, to understand the accuracy of this method under differing excited state structures. The

first system (Figure 5.5A) is a standard excitonic model, featuring downhill energy transfer between three electronic excited states. All states are dipole allowed from the ground state and have a ground state recovery time τ_g that is at least an order of magnitude higher than the energy transfer times. The second system (Figure 5.5B) is the dark state system, where a fourth electronic state is added with no transition dipole moment between the state and the ground state. Excitons are allowed to transfer between this state and the three bright excited electronic states, however, so its presence will affect the EET kinetics of the three bright excitons. In this analysis, we include systems with a dark state between excitons 1 and 2 and between excitons 2 and 3 and show that the dark state only affects the extracted kinetics of adjacent excitons. In the third system (Figure 5.5C), a vibrational energy level is added to each excited state whose energy gap is resonant with the adjacent exciton energy gap. In this system, vibrational relaxation within one exciton will create below diagonal cross peak signals that constructively interfere with EET signals.

To test the principle assumptions of this method that the excited state absorption and coherence pathways can be ignored, we characterize the accuracy of the standard system parameters when the relative contribution the signal strength of excited state absorption and coherence pathways is increased (Figure 5.6). This is done for excited state absorption pathways by increasing the dipole ratio $\frac{\mu_{fe}}{\mu_{eg}}$ and for coherence pathways by increasing the dephasing time. In the latter case, dephasing times in the hundreds of femtoseconds range (which are typical dephasing times for vibrational and vibronic coherences [39–41]) will interfere with the exponential pathways involving energy transfer. The presence of long-lived coherent signals observed in multiple photosynthetic systems [6, 42, 43] might affect the time constant extraction.

Figure 5.6A shows the error in the standard three exciton system as the $\frac{\mu_{fe}}{\mu_{eg}}$ dipole ratio ranges from zero to one. In most cases, the error falls below 15% when the dipole ratio is less than 0.6, which is well below the bounds of most molecular systems, particularly when

the effective ratio of signal contribution is further minimized by lifetime broadening. Figure 5.6B shows the error as the dephasing time for excited state coherences is increased from below 100 fs to 500 fs. However, the dephasing time has little effect on the accuracy for any of the three EET time constants. The coherence pathways modulate the signal in the waiting time, but they do little to affect the monotonic signal kinetics and therefore the exponential fits. This result will hold true for both excited state electronic or vibronic coherences and ground state vibrational coherences. We conclude that the effect of interfering excited state absorption and coherence pathways does not disrupt the accuracy of the analysis and that our initial assumptions are valid.

We now compare the method's accuracy for the systems shown in Figure 5.5 using multiple kinetic schemes for energy transfer. For the standard system, we find that the method is accurate for energy transfer systems with subpicosecond kinetics, as all but one time constant is fit to within 15% accuracy. The τ_{31} time constants are all fit within 10% accuracy, and the τ_{21} constants are all extracted within 5% accuracy. In schemes with picosecond energy transfer constants, the method tends to inaccurately calculate the slow time constant with errors above 20%. However, the accuracy of the subpicosecond time constants remains within 15%. This effect is likely due to the regression more accurately fitting signals that evolve several e-folds through the waiting time (as experimental timeframes typically range from 0 to 2000 fs). We should note that for the standard system, averaging over multiple time intervals does not significantly improve the accuracy of the method.

We find that dark states only affect the accuracy of the time constants for adjacent excitons that are directly involved in energy transfer with the dark states. For each scheme, the energy transfer to (τ_{2d}) and from (τ_{d1}) the dark state is changed to test how the dark state kinetics affect the method's accuracy. All τ_{21} errors are greater than 15%. This error is due to the kinetic sink effect between excitons 2 and 1. However, τ_{31} and τ_{32} remain accurate for all schemes where energy is allowed to flow to and from the dark state, with many of

the errors falling below 5%. This result is notable because the presence of dark states on lower exciton manifolds does not disrupt the accuracy of the calculation for higher excitonic states despite the fact that the fit to τ_{31} and τ_{32} relies on knowledge of τ_{21} (see Section 5.1). In a model where a dark state is added between excitons 2 and 3, τ_{21} remains accurate for all kinetic schemes within 5%. However, τ_{32} and τ_{31} are each off by >30% for every scheme for the same kinetic sinking effect described above. In the method, τ_{31} and τ_{32} are simultaneously calculated to reproduce the time constant of the subtracted signal (see Figure 5.3, step 7). An error in one time constant due to the kinetic trap would therefore introduce an error in the other time constant. For both dark state systems, averaging over multiple time intervals does not improve the method accuracy. We should note that the method is only accurate when excitons are allowed to flow in and out of the dark state. The method is highly inaccurate for all time constants when energy does not flow back. Thus, in systems containing dark states that couple to the excitonic states, knowledge of the electronic states and their couplings must be known *a priori* to know which calculated time constants will be accurate.

In the final step of the analysis, multiple time intervals are averaged to minimize errors due to arbitrary choice of waiting time intervals (Figure 5.3, step 8). This step does not improve the accuracy of the standard and dark state systems, but it markedly improves the accuracy of the vibrational system. For multiple kinetic schemes when the slow relaxation of resonant vibrations interferes with below diagonal energy transfer cross peaks, the analysis method remains accurate to 10% for all time constants after averaging over multiple waiting time intervals. For the vibrational system, we find that the fits with the smallest least squares fit to the subtracted signal and those which most accurately extract the energy transfer time constants occur when shorter time intervals are averaged (e.g. from 50–1050 fs to 50 –1775 fs). This range is long enough to capture multiple energy transfer e-folds but short enough to minimize the effect of picosecond signal changes due to vibrational relaxation. This result is

in contrast to the purely electronic standard and dark state kinetic systems, where the smallest least squares error and most accurate time constant fits occur over larger time intervals. In experimental molecular spectra, there will be slow signals due to vibrational relaxation and other nuclear motion not completely removed from the signal averaging [44, 45]. It is necessary to average over the time intervals to most accurately extract the kinetic time constants. The need to average over shorter time intervals could therefore show the presence of interfering Stokes shift signals in experimental 2D measurements. For all system types, the error in the time constant τ_{21} is smaller than τ_{31} and τ_{32}. (Tables S7-10). This result is due to a combination of two effects. The first is the relatively smaller number of kinetic pathways involving 2-1 energy transfer. For the 2 diagonal and 2-1 cross peak, there are no competing kinetic pathways that influence the signal. Conversely, exciton migration through both the exciton 3-2-1 pathway and the direct 3-1 pathway both cause the 3 diagonal to decrease and the 3-1 cross peak to increase with time. The competing pathways amplify small errors in the analysis because the τ_{31} and τ_{32} time constants because both τ_{31} and τ_{32} are fit simultaneously, as described above. The second effect is the approximation of the exciton 3 loss pathway (Figure 5.3, step 4). The τ_{3L} time constant is estimated as the short time constant of the diagonal. The loss rate constrains τ_{32} and τ_{31} because the sum $k_{32}+k_{31}$ must equal k_{3L}, but other Feynman pathways such as the ESA pathways and the ground state bleach recovery contribute to signal loss on the 3 diagonal. This approximation thus limits the possibility of reproducing the subtracted signal with complete accuracy. However, we have shown that the time constants are still fit within 15% accuracy despite these limitations.

5.3 Discussion

The current method applies to energy transfer systems using a traditional all parallel two-dimensional electronic spectroscopy pulse sequence. We now describe how the analysis can be

extended to solid state semiconducting materials and to isolate the chiral dynamics initiated by novel pulse sequences.

5.3.1 Many-Body Interactions in Solid-State Materials

In solid state semiconducting materials, high carrier excitation densities generated in optical experiments can lead to nontrivial interactions among excited state species (e.g. charge carriers and photoexcited excitons) that determine the optical response. These interactions lead to excitation-induced effects that manifest in characteristic lineshapes, spectral shifts, peak broadening, and higher-lying bound states [46, 47]. Incorporating many-body effects such as excitation-induced shifts and dephasing can lead to non-perfect cancellation of photoinduced absorption (PIA) and GSB signal pathways between coupled transitions and explain the presence of coupling cross-peaks, for example [48]. These effects can be incorporated in model 2D spectra by modifying the transition frequency and dephasing time as a function of excitation density to compare to experimental spectra. Feynman diagrams that explicitly note and account for these many-body interactions are required to fully describe these effects in such systems.

In semiconducting monolayer transition metal dichalcogenides (TMDs) such as MoS2, dynamic screening by photoexcited charge carriers leads to changes in the exciton binding energy and bandgap renormalization. These competing processes result in transient exciton energy level shifts and manifest as PIA features from the ground state to the renormalized optical transition in transient absorption and two-dimensional spectroscopic experiments on the sub-100 fs timescale [19, 49, 50]. A proposed 'expanded' Feynman pathway contributing to these observed signals is shown in Figure 5.7. Here, the presence of photoexcited excitons or charge carriers from the pump excitation leads to a dynamic change in its transition energy during the waiting time, and the probe pulse induces a transition from the ground state to this newly shifted level. In the absence of many-body effects, $g = g \sim$ energetically, and

the many-body PIA and GSB pathways cancel; the dynamic redshifted PIA feature is therefore observable due to the time-dependent spectral shift arising from the dynamic screening leading to bandgap renormalization. In modeling or analyzing experimental 2D spectra, expanded Feynman diagrams with specified interaction energy can be included to account for such dynamic spectral shifts in addition to instantaneous multi-particle correlations such as biexciton states. Electrochromic shifts in molecular systems can lead to similar transient energetic shifts and PIA features. To account for these band-shift PIA signals in 2DES of bacterial reaction center, Zigmantas and coworkers developed additional 're-excitation' pathways which are expanded to include product states of two species [51]. Explicit many-body Feynman diagrams have also been employed in fifth-order 2D experiments probing exciton-exciton annihilation [52]. Because the signals seen in 2D spectroscopic experiments are the interference of all possible Feynman pathways, delineating the possible many-body Feynman pathways will aid in both interpreting, predicting, and analyzing 2D spectroscopic signals.

5.3.2 Isolation of 'Handed' Energy Transfer Time Constants from Two-Dimensional Circular Dichroism Spectroscopy

Manipulation of the polarization of light can be a useful tool for further isolation of particular material response pathways in more complicated systems [53, 54]. Generally, the orientational factors for a particular pulse sequence can be calculated to predict its effect on different pathways, as shown by Dreyer et al [55]. Because different polarization configurations will interrogate different tensor elements of the third-order signal, Feynman pathways of interest can be suppressed or enhanced depending on the relative polarization of the beams and the orientations of transition dipoles of interest. Of particular interest is how this method can be applied to the chiral response of a system. When measuring only an odd tensor of the third order response, where one interaction is orthogonal to the other three, all electric dipolar signals go to zero, leaving only chiral signals and some much weaker multipolar signals [56–60].

In the context of two-dimensional Fourier transform spectroscopy, one can make a correlation map with chiral resolution on either the excitation (chiral pump) or detection (chiral probe) axes, as shown in Figure 5.8. The so-called chiral resolution comes from the creation of a chiral grating in the sample such that the signal is the result of the difference between left (LCP) and right circularly polarized (RCP) light. The generated signals can be interpreted as circular dichroism experiments with femtosecond time resolution [57, 58].

We consider a simple three level system with a shared ground state, where the J=±1 angular momentum states of each excited state are nondegenerate because of symmetry breaking due to the chirality of the molecule. Figure 5.8B shows mock chiral pump and chiral probe correlation maps at a positive waiting time where energy transfer has begun. In each correlation map, there are six main features: four diagonal peaks and two cross peaks. The diagonal peaks may look slightly off-diagonal due to the LCP-RCP subtraction inherent in the pulse sequence. When considering all of the Feynman pathways which contribute to each peak (while keeping the approximation to ignore ESA and coherence pathway contributions), we find several useful dynamical symmetries emerge.

Removal of GSBR Contribution from Chiral Response

First, in the chiral probe sequence, we find that the ground state bleach recovery pathways for both the diagonal and below diagonal cross peaks have the same waiting time dynamics because the achiral pump cannot resolve differences between the J=±1 states (Figure 5.8C). The bleach recovery subtraction in this pulse configuration can thus be done with any pair of diagonal and corresponding below diagonal cross peak signals. In the chiral pump sequence, the cancellation is not as simple. In this case, the peaks retain knowledge of the J=±1 excitation state but are agnostic to the angular momentum state of the probe. However, symmetries still exist between the diagonal and cross peaks which lie on the same excitation energy. That is, the bleach recovery signal can be subtracted but only between peaks with

the same J=±1 excitation (Figure 5.8C).

Subtraction of the bleach recovery signal in chiral pulse sequences is a straightforward extension of the cancellation in the all parallel sequence. Figure 5.9 shows the stimulated emission, ground state bleach, and ground state bleach recovery pathways for the diagonal and below diagonal peaks in the chiral pump (XYXX) and chiral probe (XXXY) sequences. For the chiral probe spectra, the bleach recovery dynamics are identical for both diagonal peaks and both cross peaks (pathways e-h). This symmetry is due to the fact that both J=±1 angular momentum states in this scheme are accessed via the achiral pump. While the chiral probe selectively drives transitions to angular momentum states in t3, the dynamics of the waiting time are the same between peaks. Therefore, the bleach recovery signal can be subtracted by normalizing and subtracting the diagonal and cross peak signals. For the chiral pump sequence, the bleach recovery contribution can still be subtracted, but care must be taken to subtract the proper diagonal peak from its respective cross peak. In Figure 5.9, pathways b and d both undergo ground state bleach recovery during t_2 from the J=+1 angular momentum state. Similarly, pathways a and c undergo recovery from the J=–1 state. Therefore, the normalized peak b must be subtracted from the normalized peak d and the normalized peak a must be subtracted from the normalized peak c to properly remove the bleach recovery signal. These symmetries are due to the chiral excitation of the pump. Once the recovery signals are removed and the subtracted signals are fit, one can then proceed to numerically fit the chiral rate constants.

Chiral Rate Constants

We find that four energy transfer pathways emerge between the four J=±1 angular momentum states on the two excited states. When taking both the chiral pump and chiral probe sequences together, these four pathways appear within the four cross peaks in unique pairs (Figure 5.8D). Though their energy transfer dynamics are not immediately separable, one

could fit the four time constants after ground state bleach recovery removal and numerically solve for the chiral rate constants that reproduce these subtracted signals. Isolating these chiral rates of energy transfer gives unprecedented insight into 'handed' energy transfer and the role of chirality in ultrafast dynamics.

5.4 Conclusions

We develop and characterize a method to accurately fit two-dimensional spectra to elementary kinetic rates for multistate energy transfer systems. We simulated two-dimensional spectra for standard multiexcitonic systems undergoing energy transfer, systems comprised of dark states that act as kinetic traps for energy transfer, and systems with resonant vibrations that undergo vibrational relaxation. The method remains accurate in the efficient energy transfer regime even when the signals are convoluted by excited state absorption pathways, long-lived coherence, and interfering vibrational relaxation pathways. When dark states are present the system, the fitting is accurate for energy transfer between states that are not adjacent to the dark state. Extracting accurate kinetic information from EET systems can provide information on the subtle microscopic parameters that influence and system and allow for precise comparative analyses between systems with slight differences, such as point mutations and functional group substitutions. As such, the method is widely applicable to excitonic systems undergoing downhill population transfer.

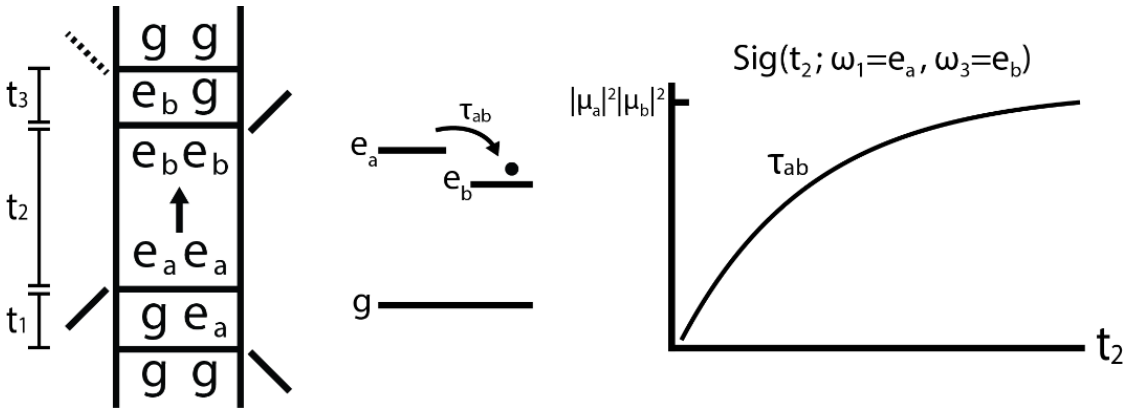

Figure 5.1: Double-sided Feynman pathway representing a dynamical subensemble that undergoes population transfer from state e_a to e_b during the waiting time, t_2. The excitation and detection axes ω_1 and ω_3 are respectively given by the bra-ket energy difference during t_1 and t_3. The signal evolution through t_2 is proportional to the population of excitation probed from e_b that began in e_a at $t_2 = 0$. As such, the pathway will evolve with the kinetics of energy transfer such that its rise time will be given by τ_{ab} and its decay will be given by the loss of e_b population, τbL. The signal strength is weighted by the transition dipole magnitudes of the four laser interactions, in this case $|\mu_a|^2|\mu_b|^2$.

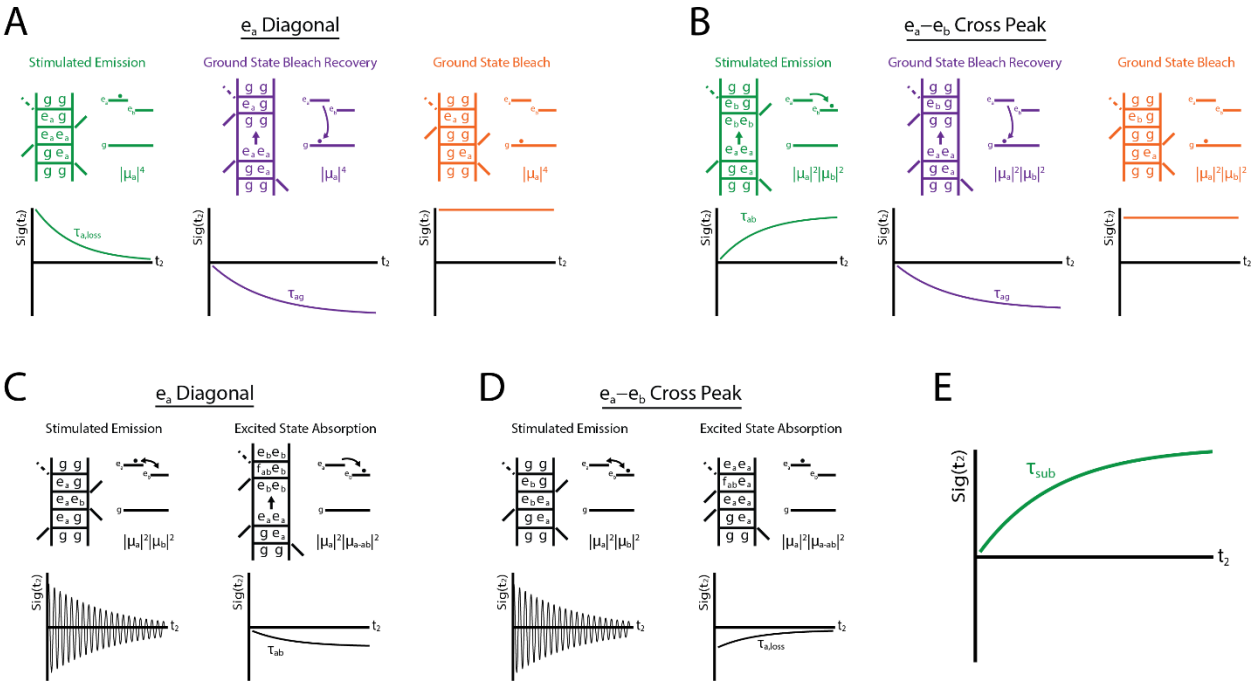

Figure 5.2: Excitonic Feynman pathways between diagonal peaks and corresponding below diagonal cross peaks possess dynamical symmetries that allow for isolation of population transfer signals. The major contributing pathways to these peaks (A, B) are stimulated emission, ground state bleach recovery, and ground state bleach signals. The ground state bleach recovery signals evolve with the same kinetics given by τ_{ag} on both peaks, but the stimulated emission pathways evolve according to their respective population transfer kinetics. The three pathways on the diagonal and cross peak have the transition dipole strength, given by $|\mu_a|^4$ for the diagonal and $|\mu_a|^2|\mu_b|^2$ for the cross peak. The pathways with relatively smaller contribution to the waiting time kinetics (C, D) are the coherence and excited state absorption pathways. These pathways are ignored as a principle assumption in this analysis. E) The normalized diagonal and cross peak signals can be subtracted to remove the bleach recovery pathway. What remains is a signal whose kinetics exclusively evolve according to population transfer. The subtracted time constant τ_{sub} can thus be used as a parameter to fit to energy transfer time constants. Note: for each rephasing pathway that undergoes population evolution during t_2, there is a corresponding nonrephasing pathway that undergoes the same waiting time dynamics, not shown here for brevity.

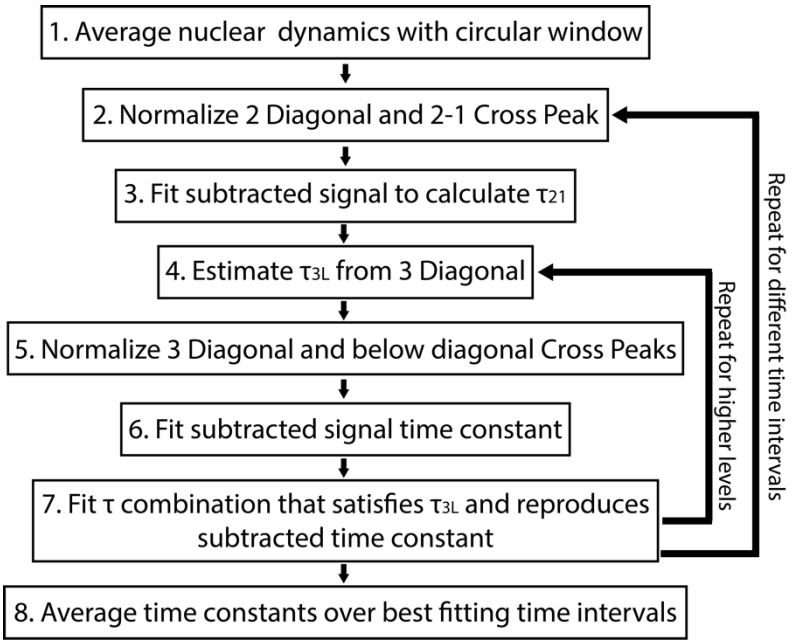

Figure 5.3: Scheme for extracting kinetic time constants from two-dimensional spectroscopic signals. Time constants are calculated from lowest to highest exciton energy. The entire procedure is repeated for multiple time intervals, and those with the best fitting subtracted time trace are averaged to generate the most accurate time constants.

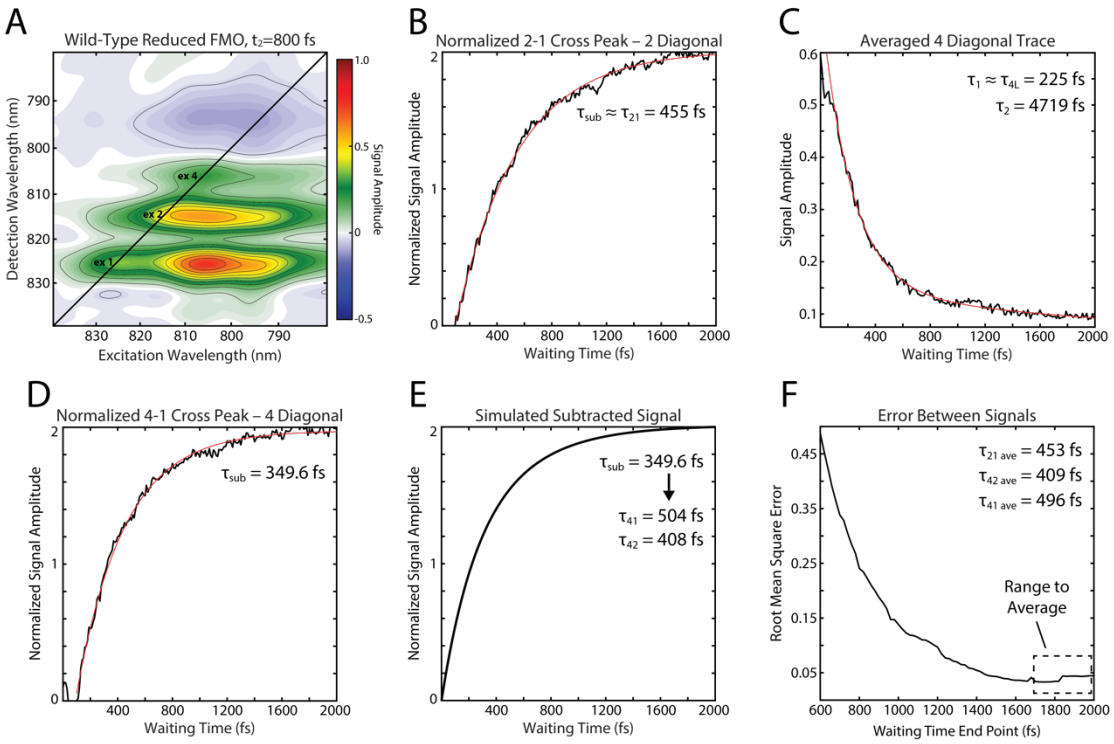

Figure 5.4: Demonstration of the analysis method using the Fenna-Matthews-Olson complex. A) Absorptive waiting time spectrum at t_2 =800 fs. Shown are the exciton 1, 2, and 4 diagonal peaks and their corresponding below diagonal cross peaks. Each peak region is averaged using a 70 cm^{-1} window. B) Fit to the normalized 2 diagonal subtracted from the normalized 2-1 cross peak traces. The monoexponential time constant is approximately equal to the τ_{21} energy transfer time constant 455 fs. C) Biexponential fit to the averaged exciton 4 diagonal trace. The first time constant is used as the 4 loss time. D) Fit to the normalized 4 diagonal subtracted from the normalized 4-1 cross peak traces. E) Simulated subtracted signal reproduces the signal time constant in panel (D) using τ_{41} =504 fs and τ_{42} =408 fs, which satisfies the constraint of τ_{4L}. F) This process is repeated using a series of waiting time ranges, and the root-mean-square error between the signals in (D) and (E) are calculated. The time constants are averaged over the lowest error region to obtain the final energy transfer time constants.

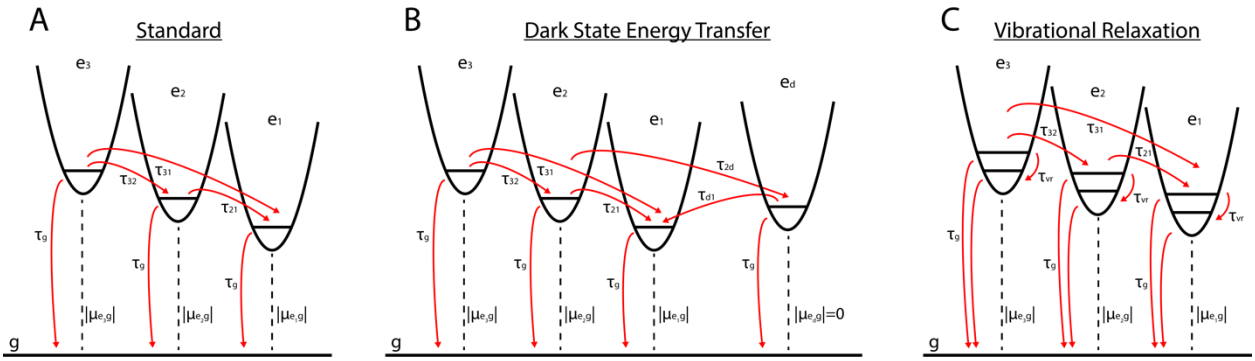

Figure 5.5: Three types of systems are used in global response calculations. A) Standard electronic system with three bright excitonic states allowing downhill energy transfer and slow relaxation to the ground state. B) Dark state system, where a fourth excitonic state is added to the standard system. This state has no oscillator strength with the ground state but still participates in downhill energy transfer with other excitons. Shown is a dark state between excitons 2 and 1, but the same analysis is also conducted using a dark state between excitons 3 and 2. C) Vibrational system, where vibrational modes resonant with the exciton energy gap are added to the standard system. Vibrational relaxation constructively interferes with below diagonal cross peak dynamics and slows the signal evolution.

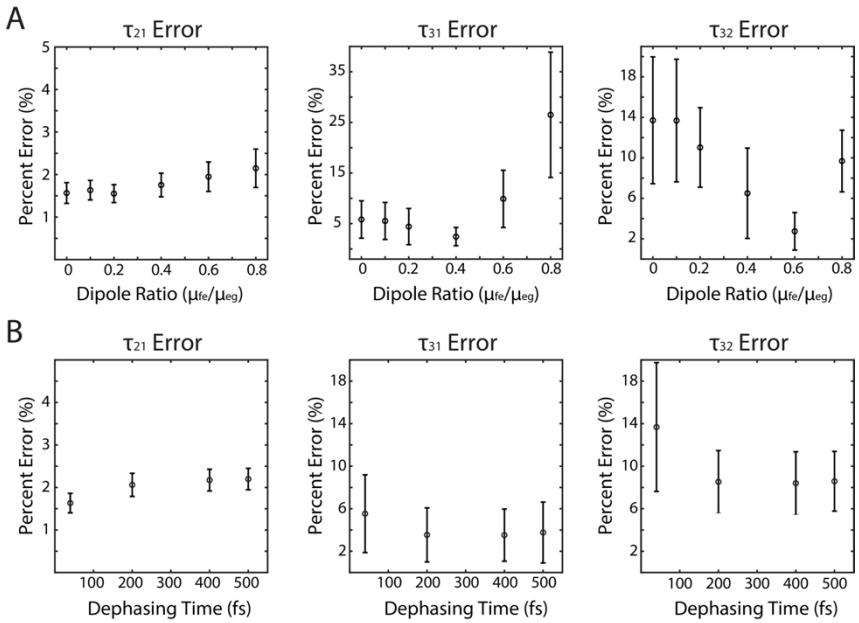

Figure 5.6: Error analysis for interfering excited state absorption and coherence pathways in the kinetic extraction method for a variety of time constants in the standard system. A) Percent error for each time constant as a function of relative transition dipole magnitude between μ_{fe} and μ_{eg}, which corresponds to the relative signal strength of the excited state absorption and ground state bleach/stimulated emission pathways, respectively. B) Percent error as a function of dephasing time for excited state electronic coherences. Long-lived coherences have little effect on the accuracy of the method because they do not contribute to monotonic signal growth or decay.

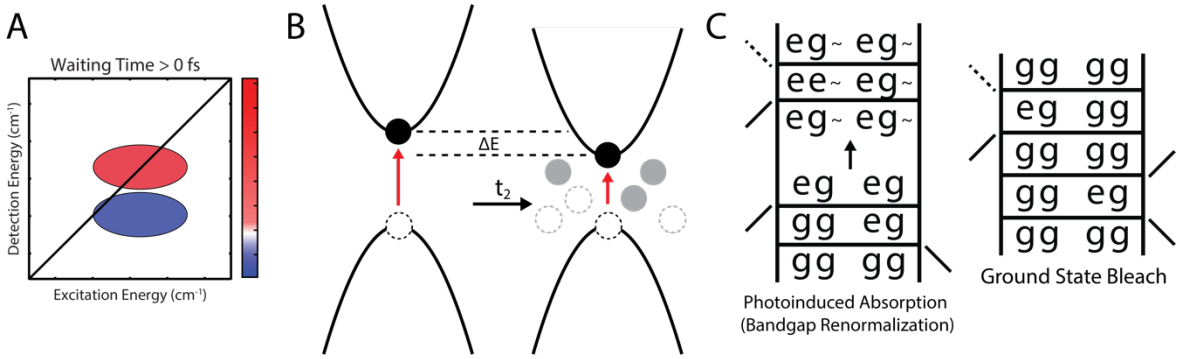

Figure 5.7: Dynamical effects in solid state materials can be described with Feynman pathways. Mock two-dimensional spectrum at $t_2 > 0$ (A) and energy diagram (B) depicting a bandgap renormalization mechanism observed in monolayer transition metal dichalcogenides [19]. Here, screening by excitations generated in the first two laser interactions dynamically alter the bandgap such that the photoinduced absorption signal imperfectly cancels with the bleach signal. C) This process can be described by 'expanded' Feynman diagrams that incorporate these many-body effects. The tilde ($\sim$) indicates the renormalization of a composite state coupled to the initial excitation.

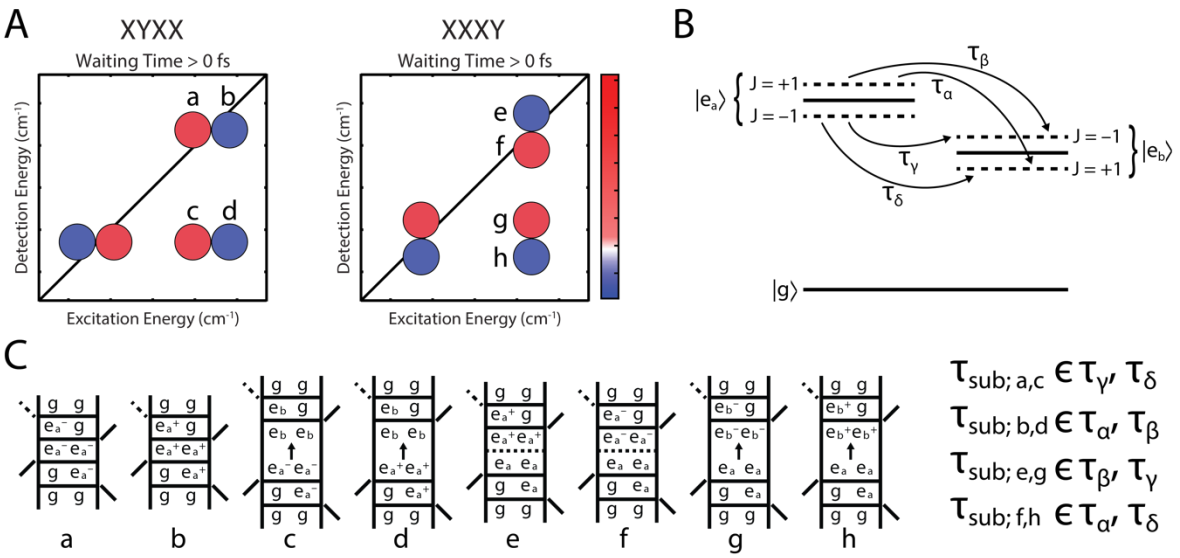

Figure 5.8: The chiral response of a system can be tracked with odd pulse sequences [57]. A) Mock two-dimensional spectra depicting the chiral dynamics using chiral pump (XYXX) and chiral probe (XXXY) sequences. B) Chirality breaks the degeneracy between angular momentum states of a molecule. Energy transfer can occur between states of the same (τ_α, τ_γ) or different (τ_β, τ_δ) angular momentum. C) Feynman pathways showing how chiral energy transfer can be either pumped or probed after the bleach recovery subtraction. Here, the $\pm$ symbols represent the angular momentum state that is either pumped or probed. The absence of such symbols indicates that the system is pumped/probed in both angular momentum states. The dashed lines in pathways e and f indicate that while the system is pumped in both angular momentum states, it is only probed from one state. Each of the four subtracted signals is comprised of a unique pair of energy transfer time constants, allowing for fitting procedures to isolate the chiral rate constants for energy transfer.

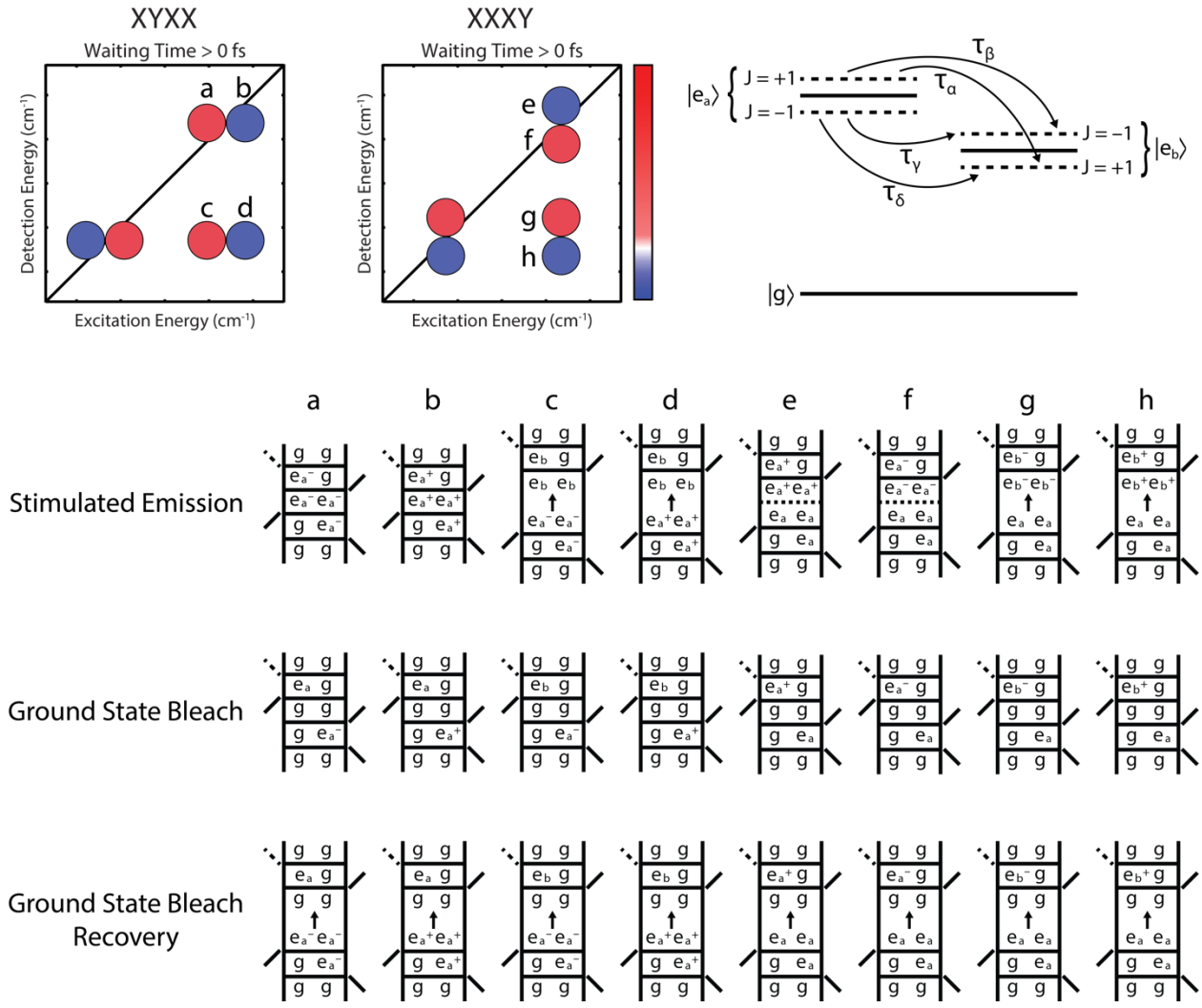

Figure 5.9: Stimulated emission, ground state bleach, and ground state bleach recovery population pathways for the chiral response. The XYXX and XXXY labels represent the chiral pump and chiral probe spectra, respectively. (Same system as Figure 5.8, but with additional population Feynman pathways added.)

REFERENCES

[1] Jacob S Higgins, Anna R. Dardia, Chidera J. Ndife, Lawson T. Lloyd, Elizabeth M. Bain, and Gregory S. Engel. Leveraging dynamical symmetries in two-dimensional electronic spectra to extract population transfer pathways. *submitted*, 2022.

[2] Minhaeng Cho, Harsha M Vaswani, Tobias Brixner, Jens Stenger, and Graham R Fleming. Exciton analysis in 2d electronic spectroscopy, 2005.

[3] Jonggu Jeon, Sungnam Park, and Minhaeng Cho. *Two-dimensional Optical Spectroscopy: Theory and Experiment*. John Wiley Sons, Ltd, 2010.

[4] Gregory D Scholes, Graham R Fleming, Lin X Chen, Alán Aspuru-Guzik, Andreas Buchleitner, David F Coker, Gregory S Engel, Rienk Van Grondelle, Akihito Ishizaki, David M Jonas, et al. Using coherence to enhance function in chemical and biophysical systems. *Nature*, 543(7647):647–656, 2017.

[5] Lili Wang, Marco A Allodi, and Gregory S Engel. Quantum coherences reveal excited-state dynamics in biophysical systems. *Nature Reviews Chemistry*, 3(8):477–490, 2019.

[6] Gitt Panitchayangkoon, Dugan Hayes, Kelly A Fransted, Justin R Caram, Elad Harel, Jianzhong Wen, Robert E Blankenship, and Gregory S Engel. Long-lived quantum coherence in photosynthetic complexes at physiological temperature. *Proceedings of the National Academy of Sciences*, 107(29):12766–12770, 2010.

[7] Jakub Dostál, Jakub Pšenčík, and Donatas Zigmantas. In situ mapping of the energy flow through the entire photosynthetic apparatus. *Nature Chemistry*, 8(7):705–710, 2016.

[8] Hong-Guang Duan, Valentyn I Prokhorenko, Richard J Cogdell, Khuram Ashraf, Amy L Stevens, Michael Thorwart, and RJ Dwayne Miller. Nature does not rely on long-lived

electronic quantum coherence for photosynthetic energy transfer. *Proceedings of the National Academy of Sciences*, 114(32):8493–8498, 2017.

[9] Franklin D Fuller, Jie Pan, Andrius Gelzinis, Vytautas Butkus, S Seckin Senlik, Daniel E Wilcox, Charles F Yocum, Leonas Valkunas, Darius Abramavicius, and Jennifer P Ogilvie. Vibronic coherence in oxygenic photosynthesis. *Nature chemistry*, 6(8):706–711, 2014.

[10] Minjung Son, Alberta Pinnola, Roberto Bassi, and Gabriela S Schlau-Cohen. The electronic structure of lutein 2 is optimized for light harvesting in plants. *Chem*, 5(3):575–584, 2019.

[11] Minjung Son, Alberta Pinnola, Samuel C Gordon, Roberto Bassi, and Gabriela S Schlau-Cohen. Observation of dissipative chlorophyll-to-carotenoid energy transfer in light-harvesting complex ii in membrane nanodiscs. *Nature communications*, 11(1):1–8, 2020.

[12] Tobias Brixner, Jens Stenger, Harsha M Vaswani, Minhaeng Cho, Robert E Blankenship, and Graham R Fleming. Two-dimensional spectroscopy of electronic couplings in photosynthesis. *Nature*, 434(7033):625–628, 2005.

[13] Philip JM Johnson, Marwa H Farag, Alexei Halpin, Takefumi Morizumi, Valentyn I Prokhorenko, Jasper Knoester, Thomas LC Jansen, Oliver P Ernst, and RJ Dwayne Miller. The primary photochemistry of vision occurs at the molecular speed limit. *The Journal of Physical Chemistry B*, 121(16):4040–4047, 2017.

[14] Samer Gozem, Philip JM Johnson, Alexei Halpin, Hoi Ling Luk, Takefumi Morizumi, Valentyn I Prokhorenko, Oliver P Ernst, Massimo Olivucci, and RJ Dwayne Miller. Excited-state vibronic dynamics of bacteriorhodopsin from two-dimensional electronic photon echo spectroscopy and multiconfigurational quantum chemistry. *The Journal of Physical Chemistry Letters*, 11(10):3889–3896, 2020.

[15] Lili Wang, Graham B Griffin, Alice Zhang, Feng Zhai, Nicholas E Williams, Richard F Jordan, and Gregory S Engel. Controlling quantum-beating signals in 2d electronic spectra by packing synthetic heterodimers on single-walled carbon nanotubes. *Nature Chemistry*, 9(3):219–225, 2017.

[16] Sara H Sohail, John P Otto, Paul D Cunningham, Young C Kim, Ryan E Wood, Marco A Allodi, Jacob S Higgins, Joseph S Melinger, and Gregory S Engel. Dna scaffold supports long-lived vibronic coherence in an indodicarbocyanine (cy5) dimer. *Chemical science*, 11(32):8546–8557, 2020.

[17] Franz Milota, Valentyn I Prokhorenko, Tomas Mancal, Hans von Berlepsch, Oliver Bixner, Harald F Kauffmann, and Jurgen Hauer. Vibronic and vibrational coherences in two-dimensional electronic spectra of supramolecular j-aggregates. *The Journal of Physical Chemistry A*, 117(29):6007–6014, 2013.

[18] James Lim, David Paleček, Felipe Caycedo-Soler, Craig N Lincoln, Javier Prior, Hans Von Berlepsch, Susana F Huelga, Martin B Plenio, Donatas Zigmantas, and Jürgen Hauer. Vibronic origin of long-lived coherence in an artificial molecular light harvester. *Nature communications*, 6(1):1–7, 2015.

[19] Ryan E Wood, Lawson T Lloyd, Fauzia Mujid, Lili Wang, Marco A Allodi, Hui Gao, Richard Mazuski, Po-Chieh Ting, Saien Xie, Jiwoong Park, et al. Evidence for the dominance of carrier-induced band gap renormalization over biexciton formation in cryogenic ultrafast experiments on mos2 monolayers. *The Journal of Physical Chemistry Letters*, 11(7):2658–2666, 2020.

[20] Christopher L Smallwood and Steven T Cundiff. Multidimensional coherent spectroscopy of semiconductors. *Laser & Photonics Reviews*, 12(12):1800171, 2018.

[21] Shaul Mukamel. *Principles of nonlinear optical spectroscopy*. Number 6. Oxford University Press on Demand, 1999.

[22] Andrei Tokmakoff. Time dependent quantum mechanics and spectroscopy, 2014.

[23] Sean T Roberts, Joseph J Loparo, and Andrei Tokmakoff. Characterization of spectral diffusion from two-dimensional line shapes. *The Journal of chemical physics*, 125(8):084502, 2006.

[24] Kyungwon Kwak, Sungnam Park, Ilya J Finkelstein, and Michael D Fayer. Frequency-frequency correlation functions and apodization in two-dimensional infrared vibrational echo spectroscopy: A new approach. *The Journal of chemical physics*, 127(12):124503, 2007.

[25] Emily E Fenn and MD Fayer. Extracting 2d ir frequency-frequency correlation functions from two component systems. *The Journal of chemical physics*, 135(7):074502, 2011.

[26] Marco A Allodi, John P Otto, Sara H Sohail, Rafael G Saer, Ryan E Wood, Brian S Rolczynski, Sara C Massey, Po-Chieh Ting, Robert E Blankenship, and Gregory S Engel. Redox conditions affect ultrafast exciton transport in photosynthetic pigment–protein complexes. *The Journal of Physical Chemistry Letters*, 9(1):89–95, 2018.

[27] Erling Thyrhaug, Karel Zidek, Jakub Dostál, David Bína, and Donatas Zigmantas. Exciton structure and energy transfer in the fenna–matthews–olson complex. *The Journal of Physical Chemistry Letters*, 7(9):1653–1660, 2016.

[28] Jakub Dostál, Barbora Benešová, and Tobias Brixner. Two-dimensional electronic spectroscopy can fully characterize the population transfer in molecular systems. *The Journal of Chemical Physics*, 145(12):124312, 2016.

[29] Peter Hamm and Martin Zanni. *Concepts and methods of 2D infrared spectroscopy*. Cambridge University Press, 2011.

[30] Robert Silbey. Description of quantum effects in the condensed phase. *Procedia Chemistry*, 3(1):188–197, 2011.

[31] Karthik Gururangan and Elad Harel. Coherent and dissipative quantum process tensor reconstructions in two-dimensional electronic spectroscopy. *The Journal of Chemical Physics*, 150(16):164127, 2019.

[32] Jacob S Higgins, Lawson T Lloyd, Sara H Sohail, Marco A Allodi, John P Otto, Rafael G Saer, Ryan E Wood, Sara C Massey, Po-Chieh Ting, Robert E Blankenship, et al. Photosynthesis tunes quantum-mechanical mixing of electronic and vibrational states to steer exciton energy transfer. *Proceedings of the National Academy of Sciences*, 118(11), 2021.

[33] RW Boyd and BR Masters. Nonlinear optics 3rd edn (new york: Academic). 2008.

[34] Bernard Cohen-Tannoudji, C. D. and Frank Laloe. *Quantum Mechanics*. Wiley, 1991.

[35] Mino Yang and Graham R Fleming. Third-order nonlinear optical response of energy transfer systems. *The Journal of chemical physics*, 111(1):27–39, 1999.

[36] Michael D. Harris, D. C. B. *Symmetry and Spectroscopy: An Introduction to Vibrational and Electronic Spectroscopy*. University Press, Inc, 1978.

[37] Sara H Sohail, Peter D Dahlberg, Marco A Allodi, Sara C Massey, Po-Chieh Ting, Elizabeth C Martin, C Neil Hunter, and Gregory S Engel. Communication: Broad manifold of excitonic states in light-harvesting complex 1 promotes efficient unidirectional energy transfer in vivo. *The Journal of Chemical Physics*, 147(13):131101, 2017.

[38] Peter D Dahlberg, Po-Chieh Ting, Sara C Massey, Marco A Allodi, Elizabeth C Martin, C Neil Hunter, and Gregory S Engel. Mapping the ultrafast flow of harvested solar energy in living photosynthetic cells. *Nature communications*, 8(1):1–7, 2017.

[39] Jacob S Higgins, William R Hollingsworth, Lawson T Lloyd, and Gregory S Engel. Quantum coherence in chemical and photobiological systems. In *Emerging Trends in Chemical Applications of Lasers*, pages 411–436. ACS Publications, 2021.

[40] Niklas Christensson, Harald F Kauffmann, Tonu Pullerits, and Tomas Mancal. Origin of long-lived coherences in light-harvesting complexes. *The Journal of Physical Chemistry B*, 116(25):7449–7454, 2012.

[41] Shu-Hao Yeh, Ross D Hoehn, Marco A Allodi, Gregory S Engel, and Sabre Kais. Elucidation of near-resonance vibronic coherence lifetimes by nonadiabatic electronic-vibrational state character mixing. *Proceedings of the National Academy of Sciences*, 116(37):18263–18268, 2019.

[42] Gregory S Engel, Tessa R Calhoun, Elizabeth L Read, Tae-Kyu Ahn, Tomáš Mančal, Yuan-Chung Cheng, Robert E Blankenship, and Graham R Fleming. Evidence for wavelike energy transfer through quantum coherence in photosynthetic systems. *Nature*, 446(7137):782–786, 2007.

[43] Margherita Maiuri, Evgeny E Ostroumov, Rafael G Saer, Robert E Blankenship, and Gregory D Scholes. Coherent wavepackets in the fenna–matthews–olson complex are robust to excitonic-structure perturbations caused by mutagenesis. *Nature chemistry*, 10(2):177–183, 2018.

[44] Tihana Mirkovic, Evgeny E Ostroumov, Jessica M Anna, Rienk Van Grondelle, and Gregory D Scholes. Light absorption and energy transfer in the antenna complexes of photosynthetic organisms. *Chemical reviews*, 117(2):249–293, 2017.

[45] Vladimir I Novoderezhkin and Rienk van Grondelle. Physical origins and models of energy transfer in photosynthetic light-harvesting. *Physical Chemistry Chemical Physics*, 12(27):7352–7365, 2010.

[46] Christopher L Smallwood and Steven T Cundiff. Multidimensional coherent spectroscopy of semiconductors. *Laser & Photonics Reviews*, 12(12):1800171, 2018.

[47] Galan Moody, Chandriker Kavir Dass, Kai Hao, Chang-Hsiao Chen, Lain-Jong Li, Akshay Singh, Kha Tran, Genevieve Clark, Xiaodong Xu, Gunnar Berghäuser, et al. Intrinsic homogeneous linewidth and broadening mechanisms of excitons in monolayer transition metal dichalcogenides. *Nature communications*, 6(1):1–6, 2015.

[48] Liang Guo, Meng Wu, Ting Cao, Daniele M Monahan, Yi-Hsien Lee, Steven G Louie, and Graham R Fleming. Exchange-driven intravalley mixing of excitons in monolayer transition metal dichalcogenides. *Nature Physics*, 15(3):228–232, 2019.

[49] Eva AA Pogna, Margherita Marsili, Domenico De Fazio, Stefano Dal Conte, Cristian Manzoni, Davide Sangalli, Duhee Yoon, Antonio Lombardo, Andrea C Ferrari, Andrea Marini, et al. Photo-induced bandgap renormalization governs the ultrafast response of single-layer mos2. *ACS nano*, 10(1):1182–1188, 2016.

[50] Paul D Cunningham, Aubrey T Hanbicki, Kathleen M McCreary, and Berend T Jonker. Photoinduced bandgap renormalization and exciton binding energy reduction in ws2. *ACS nano*, 11(12):12601–12608, 2017.

[51] Eglė Bukartė, David Paleček, Petra Edlund, Sebastian Westenhoff, and Donatas Zigmantas. Dynamic band-shift signal in two-dimensional electronic spectroscopy: A case of bacterial reaction center. *The Journal of Chemical Physics*, 154(11):115102, 2021.

[52] Jakub Dostál, Franziska Fennel, Federico Koch, Stefanie Herbst, Frank Würthner, and Tobias Brixner. Direct observation of exciton–exciton interactions. *Nature communications*, 9(1):1–8, 2018.

[53] Elizabeth L Read, Gregory S Engel, Tessa R Calhoun, Tomáš Mančal, Tae Kyu Ahn, Robert E Blankenship, and Graham R Fleming. Cross-peak-specific two-

dimensional electronic spectroscopy. *Proceedings of the National Academy of Sciences*, 104(36):14203–14208, 2007.

[54] Martin T Zanni, Nien-Hui Ge, Yung Sam Kim, and Robin M Hochstrasser. Two-dimensional ir spectroscopy can be designed to eliminate the diagonal peaks and expose only the crosspeaks needed for structure determination. *Proceedings of the National Academy of Sciences*, 98(20):11265–11270, 2001.

[55] Jens Dreyer, Andrew M Moran, and Shaul Mukamel. Tensor components in three pulse vibrational echoes of a rigid dipeptide. *Bulletin of the Korean Chemical Society*, 24(8):1091–1096, 2003.

[56] Darius Abramavicius and Shaul Mukamel. Chirality-induced signals in coherent multi-dimensional spectroscopy of excitons. *The Journal of chemical physics*, 124(3):034113, 2006.

[57] Andrew F Fidler, Ved P Singh, Phillip D Long, Peter D Dahlberg, and Gregory S Engel. Dynamic localization of electronic excitation in photosynthetic complexes revealed with chiral two-dimensional spectroscopy. *Nature communications*, 5(1):1–6, 2014.

[58] D. I. Holdaway, E. Collini, and A. Olaya-Castro. Isolating the chiral contribution in optical two-dimensional chiral spectroscopy using linearly polarized light. *Opt Express*, 25(6):6383–6401.

[59] D. Abramavicius and S. Mukamel. Coherent third-order spectroscopic probes of molecular chirality. *J Chem Phys*, 122(13):134305.

[60] Darius Abramavicius, Wei Zhuang, and Shaul Mukamel. Probing molecular chirality via excitonic nonlinear response. *Journal of Physics B: Atomic, Molecular and Optical Physics*, 39(24):5051–5066, 2006.

CHAPTER 6

FUTURE DIRECTIONS

There is much more to do in the fields of chiral dynamics and novel ultrafast spectroscopic instrument design. Looking at the ultrafast dynamics behind chiral aggregates composed of achiral monomers can give insight into the excitonic chirality that arises from interchromophore coupling of electric transition dipoles. Chiral nanomaterials is a growing discipline with numerous applications but their chiral dynamics are yet to be investigated. Realizing new surface specific third order nonlinear techniques would open the door for groundbreaking surface and interface science. And lastly, this section describes a new type of mixed electronic and vibrational spectroscopy which is theoretically capable of interrogating nonadiabatic dynamics in a new and information-rich way.

6.1 Ultrafast Chiral Dynamics of Chiral Aggregates of Achiral Porphyrins

Chiral aggregates are of great interest as a model system for understanding light harvesting and chiral memory [1–5]. These specific porphyrin aggregates can form either spontaneously or by the transfer and retention of chiral information from a template. These processes have been studied extensively but the dynamics behind their steady state circular dichroism measurements have not been investigated to date. Understanding how geometric chiral memory affects electronic chiral memory is one of the goals of studying this sample. The spontaneous formation of these aggregates can happen on a timescale of hours such that we can potentially track how their ultrafast dynamics change at different points in this process. If we can map something as simple as aggregate length onto electronic chiral memory, then we can begin the process of learning how to manipulate those dynamics.

6.2 Interrogating the Origin of Circular Dichroism Signals in Chiral Ligand Capped Quantum Dots Using Two-Dimensional Circular Dichroism Spectroscopy

Chiral nanomaterials have been of great interest for a multitude of applications including biosensing, enantioselective catalysis, and optoelectronics [6–9]. Quantum dots, which themselves are achiral, can exhibit an induced chirality when capped with chiral ligands such as cysteines [7, 8, 10]. The origins of this induced chirality is highly debated. Theories include mixing between the ligand HOMO and the dot valence band, as well as a surface reorganization upon ligand exchange [7, 8]. As linear circular dichroism is inherently a steady state measurement, it is probable that more information lies in the dynamics which are behind those signals. Measuring the ultrafast chiral dynamics of these quantum dots can lead to new insights into the origin of these signals. Along with the dynamics, frequency-frequency correlation maps give information about the couplings between states, providing much sought-after information about the potential electronic coupling between ligand and dot states [11, 12]. In addition, line shape analyses can uncover the origins of inhomogeneity in these systems [13].

6.3 Surface Specific 2DES of TIPS-Pentacene Self Assemblies

Recently, Zanni and coworkers [14] have theoretically demonstrated that the pulse sequences used to eliminate achiral background and reveal chiral dynamics can also be used to obtain surface specific signals in certain samples. Restrictions to the sample include that it must be achiral, have macroscopic uniaxial and polar order at the surface, and have coupled, nonparallel transition dipoles. The result is that electric transition dipole signals survive at an interface that meets these requirements. Seeing as we have already built an instrument capable of measuring these signals in 2DCD, it follows that this would be an important

experiment to attempt.

In terms of a first sample, TIPS-pentacene makes sense as it has coupled non-parallel transition dipoles and meets the requirement of uniaxial order when self-assembled [14, 15]. Self-assembled TIPS-pentacene should then have a dipolar signal for any pulse sequence where one of the interactions is orthogonally polarized with respect to the other three. Because self-assembled TIPS-pentacene exhibits this required order across many layers, this measurement will not be surface specific, but it can stand as a proof-of-concept experiment that you can in fact get signal from an achiral sample using these polarization sequences. This would open the door to future studies at the frontier of surface science, including the electronic dynamics of buried interfaces.

6.4 Vibrationally Prepared Transient Absorption and 2DES

Understanding nonadiabatic couplings is fundamental to understanding photochemistry. Being able to predict the outcome of photochemical reactions is vital to effective solar light harvesting and clean energy generation. Several spectroscopies have been developed to try to illuminate nonadiabatic dynamics more directly [16–18]. Here I propose we take a Raman-based vibrational preparation, like what is used in Femtosecond Stimulated Raman Spectroscopy [16] (FSRS) and Two-Dimensional Electronic Raman Spectroscopy [17] (2DER) and use that to prepare a vibrational excited state that we then interrogate with either transient absorption (TA) or 2DES (see pulse sequence in Figure 6.1). In FSRS and 2DER, the Raman portion of the experiment lacks femtosecond time resolution because of the uncertainty involved in the arrival time of the second Raman interaction with the virtual state. This interaction can happen any time during the dephasing time of the vibrational coherence which essentially means they are measuring an average over that lifetime which for vibrations can last several picoseconds. For the experiment I am proposing, Vibrationally Prepared TA or 2DES (VP-TA or VP-2DES), the Raman interactions happen first and therefore are explic-

itly defined by the arrival time of the two femtosecond near infrared (NIR) Raman probes and thus femtosecond time resolution is preserved. After the first Raman interaction, at some point the second Raman process occurs, placing the system in a vibrational population. Simultaneously, a bluer visible light pulse promotes the system to an electronic excited state population. Then sometime later the system is probed by another visible light pulse to see where the vibrationally prepared electronic wavepacket ended up. Because the period of a vibration is on the order of hundreds of femtoseconds, having femtosecond resolution of this vibrational coherence time means that one can correlate the vibrational phase or momentum on the ground state with the outcome of a photochemical process. Understanding these correlations can provide vital insight into how ground state vibrational structures can be used to manipulate the outcome of photochemical reactions.

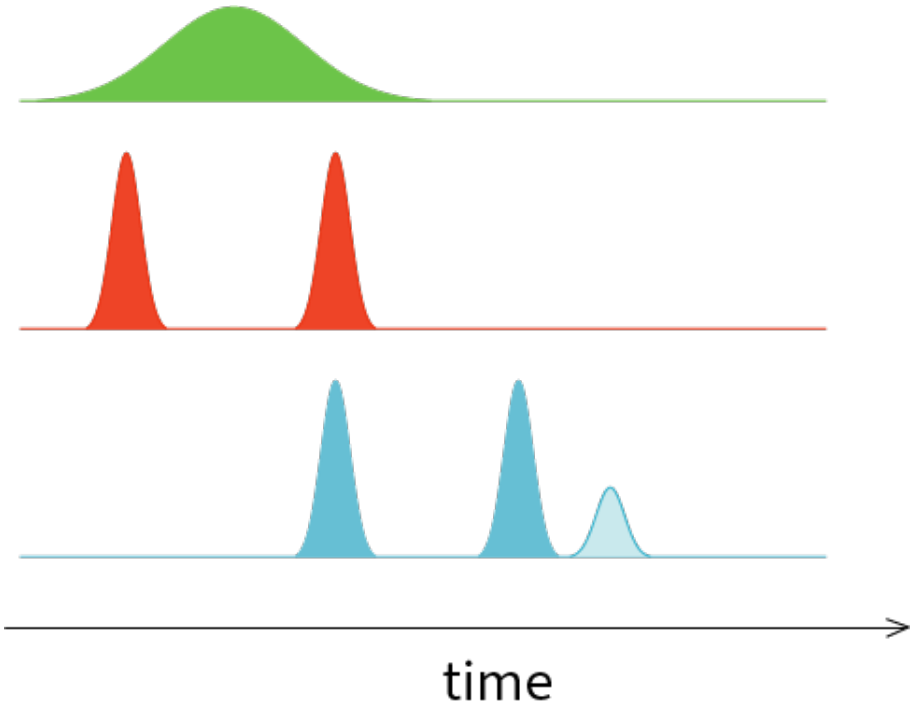

Figure 6.1: Possible pulse sequence for VP-TA and VP-2DES. Blue pulses are broadband, femtosecond visible light pulses that perform electronic excitations. The lighter blue pulse is the signal which will be in the visible light range because it will emit from an electronic coherence. The red pulses are broadband, femtosecond near infrared pulses referred to as the Raman probe pulses because they stimulate emission from the virtual state. The green pulse is the narrowband, picosecond pulse centered just blue of the Raman probe pulses and referred to as the Raman pump because it promotes the system to the virtual state. The sequence shown is for VP-TA. For VP-2DES the first blue pulse would be split in two and the time between them scanned.

REFERENCES

[1] Nakul C Maiti, Shyamalava Mazumdar, and N Periasamy. J-and h-aggregates of porphyrin- surfactant complexes: time-resolved fluorescence and other spectroscopic studies. *The Journal of Physical Chemistry B*, 102(9):1528–1538, 1998.

[2] Josep M Ribo, Joaquim Crusats, Francesc Sagués, Josep Claret, and Raimon Rubires. Chiral sign induction by vortices during the formation of mesophases in stirred solutions. *Science*, 292(5524):2063–2066, 2001.

[3] Qiuling Wang, Li Zhang, Dong Yang, Tiesheng Li, and Minghua Liu. Chiral signs of tpps co-assemblies with chiral gelators: role of molecular and supramolecular chirality. *Chemical Communications*, 52(84):12434–12437, 2016.

[4] Li Zhang, Jing Yuan, and Minghua Liu. Supramolecular chirality of achiral tpps complexed with chiral molecular films. *The Journal of Physical Chemistry B*, 107(46):12768–12773, 2003.

[5] Lizhi Zhao, Rui Xiang, Rujiang Ma, Xin Wang, Yingli An, and Linqi Shi. Chiral conversion and memory of tpps j-aggregates in complex micelles: Peg-b-pdmaema/tpps. *Langmuir*, 27(18):11554–11559, 2011.

[6] Junjun Liu, Lin Yang, Ping Qin, Shiqing Zhang, Ken Kin Lam Yung, and Zhifeng Huang. Recent advances in inorganic chiral nanomaterials. *Advanced Materials*, 33(50):2005506, 2021.

[7] Assaf Ben-Moshe, Ayelet Teitelboim, Dan Oron, and Gil Markovich. Probing the interaction of quantum dots with chiral capping molecules using circular dichroism spectroscopy. *Nano letters*, 16(12):7467–7473, 2016.

[8] Urice Tohgha, Kirandeep K Deol, Ashlin G Porter, Samuel G Bartko, Jung Kyu Choi, Brian M Leonard, Krisztina Varga, Jan Kubelka, Gilles Muller, and Milan Balaz. Ligand

induced circular dichroism and circularly polarized luminescence in cdse quantum dots. *ACS nano*, 7(12):11094–11102, 2013.

[9] Liguang Xu, Xiuxiu Wang, Weiwei Wang, Maozhong Sun, Won Jin Choi, Ji-Young Kim, Changlong Hao, Si Li, Aihua Qu, Meiru Lu, et al. Enantiomer-dependent immunological response to chiral nanoparticles. *Nature*, 601(7893):366–373, 2022.

[10] Irina V Martynenko, Anvar S Baimuratov, Victoria A Osipova, Vera A Kuznetsova, Finn Purcell-Milton, Ivan D Rukhlenko, Anatoly V Fedorov, Yurii K Gun'ko, Ute Resch-Genger, and Alexander V Baranov. Excitation energy dependence of the photoluminescence quantum yield of core/shell cdse/cds quantum dots and correlation with circular dichroism. *Chemistry of Materials*, 30(2):465–471, 2018.

[11] Justin R Caram, Haibin Zheng, Peter D Dahlberg, Brian S Rolczynski, Graham B Griffin, Dmitriy S Dolzhnikov, Dmitri V Talapin, and Gregory S Engel. Exploring size and state dynamics in cdse quantum dots using two-dimensional electronic spectroscopy. *The Journal of chemical physics*, 140(8):084701, 2014.

[12] Justin R Caram, Haibin Zheng, Peter D Dahlberg, Brian S Rolczynski, Graham B Griffin, Andrew F Fidler, Dmitriy S Dolzhnikov, Dmitri V Talapin, and Gregory S Engel. Persistent interexcitonic quantum coherence in cdse quantum dots. *The journal of physical chemistry letters*, 5(1):196–204, 2014.

[13] Eric M Janke, Nicholas E Williams, Chunxing She, Danylo Zherebetskyy, Margaret H Hudson, Lili Wang, David J Gosztola, Richard D Schaller, Byeongdu Lee, Chengjun Sun, et al. Origin of broad emission spectra in inp quantum dots: Contributions from structural and electronic disorder. *Journal of the American Chemical Society*, 140(46):15791–15803, 2018.

[14] Megan K Petti, Joshua S Ostrander, Erin R Birdsall, Miriam Bohlmann Kunz, Zachary T Armstrong, Ariel M Alperstein, and Martin T Zanni. A proposed method to obtain surface specificity with pump–probe and 2d spectroscopies. *The Journal of Physical Chemistry A*, 124(17):3471–3483, 2020.

[15] Zachary T Armstrong, Miriam Bohlmann Kunz, Andrew C Jones, and Martin T Zanni. Thermal annealing of singlet fission microcrystals reveals the benefits of charge transfer couplings and slip-stacked packing. *The Journal of Physical Chemistry C*, 124(28):15123–15131, 2020.

[16] Philipp Kukura, David W McCamant, and Richard A Mathies. Femtosecond stimulated raman spectroscopy. *Annu. Rev. Phys. Chem.*, 58:461–488, 2007.

[17] Zhengyang Zhang, Adriana Huerta-Viga, and Howe-Siang Tan. Two-dimensional electronic-raman spectroscopy. *Optics Letters*, 43(4):939–942, 2018.

[18] Thomas AA Oliver, Nicholas HC Lewis, and Graham R Fleming. Correlating the motion of electrons and nuclei with two-dimensional electronic–vibrational spectroscopy. *Proceedings of the National Academy of Sciences*, 111(28):10061–10066, 2014.

CHAPTER 7

CONCLUSIONS

Understanding how chiral materials are potentially uniquely positioned to efficiently harvest solar energy is an ongoing problem. This thesis has described the development of novel instrumentation and analysis for the study of chiral electronic dynamics to provide insight to these issues. A number of potential barriers to achieving two-dimensional circular dichroism spectroscopy that were outlined in the introduction have been addressed throughout this dissertation. First, the extremely low signal intensity associated with circular dichroism signals has been combatted by the design of a pump-probe geometry spectrometer, resulting in a larger phase matched volume and therefore the ability to excite more molecules with each laser shot than a typical BOXCAR geometry setup. Then, issues of large background were addressed by the development of fully background-free pump-probe geometry 2D spectroscopy with a temporally separated local oscillator. Polarization impurities were reduced by utilizin the natural polarization purity of birefringent crystals rather than polarizers which are imperfect. Potentially overwhelming sources of noise like shot-to-shot laser fluctuations and scatter contamination were addressed by a single shot referencing protocol and signal apodization in the Fourier domain. Then, the developement of a new model for the interpretation of chiral energy transfer dynamics was developed to bring insight to these complicated physical processes. The advances made in this work has opened new doors in the field of time-resolved circular dichroism. With this new technique, the robust study of ultrafast chiral energy transfer dynamics becomes possible.